Mapping neurotransmitter systems to the structural and functional organization of the human neocortex

Justine Y. Hansen[1], Golia Shafiei[1], Ross D. Markello[1], Kelly Smart[2,3], Sylvia M. L. Cox[4], Martin Nørgaard[5,6], Vincent Beliveau[6,7], Yanjun Wu[2,3], Jean-Dominique Gallezot[2,3], Étienne Aumont[8], Stijn Servaes[9], Stephanie G. Scala[4], Jonathan M. DuBois[10], Gabriel Wainstein[11], Gleb Bezgin[9], Thomas Funck[12], Taylor W. Schmitz[13], R. Nathan Spreng[1], Marian Galovic[14,15], Matthias J. Koepp[15], John S. Duncan[15], Jonathan P. Coles[16], Tim D. Fryer[17], Franklin I. Aigbirhio[17], Colm J. McGinnity[18], Alexander Hammers[18], Jean-Paul Soucy[1], Sylvain Baillet[1], Synthia Guimond[19,20], Jarmo Hietala[21], Marc-André Bédard[1,8], Marco Leyton[1,4], Eliane Kobayashi[1], Pedro Rosa-Neto[1,9], Melanie Ganz[6], Gitte M. Knudsen[6], Nicola Palomero-Gallagher[22], James M. Shine[11], Richard E. Carson[2,3], Lauri Tuominen[19], Alain Dagher[1], Bratislav Misic[1]*

[1]*Montréal Neurological Institute, McGill University, Montréal, QC, Canada*
[2]*Yale PET Center, Yale School of Medicine, New Haven, CT 06510, USA*
[3]*Department of Radiology and Biomedical Imaging, Yale School of Medicine, New Haven, CT 06520, USA*
[4]*Department of Psychiatry, McGill University, Montréal, QC, Canada*
[5]*Center for Reproducible Neuroscience, Department of Psychology, Stanford University, Stanford, California, USA*
[6]*Neurobiology Research Unit & CIMBI, Copenhagen University Hospital, Copenhagen, Denmark*
[7]*Medical University of Innsbruck, Department of Neurology, Innsbruck, 6020, Austria*
[8]*Cognitive Pharmacology Research Unit, UQAM, Montréal, QC, Canada*
[9]*The McGill University Research Centre for Studies in Aging, Douglas Hospital, McGill University, Montréal, QC, Canada*
[10]*Biogen Inc., Cambridge, MA, USA*
[11]*Brain and Mind Centre, The University of Sydney, Sydney, NSW, Australia*
[12]*Julich Forschungszentrum, Julich, North Rhine-Westphalia*
[13]*Department of Physiology and Pharmacology, University of Western Ontario, London, ON, Canada*
[14]*Department of Neurology, Clinical Neuroscience Center, University Hospital Zurich, Zurich, Switzerland*
[15]*Department of Clinical and Experimental Epilepsy, UCL Queen Square Institute of Neurology, London, UK; MRI Unit, Chalfont Centre for Epilepsy, UK*
[16]*Division of Anaesthesia, Department of Medicine, University of Cambridge, Addenbrooke's Hospital, Cambridge, UK*
[17]*Wolfson Brain Imaging Centre, Department of Clinical Neurosciences, University of Cambridge, Addenbrooke's Hospital, Cambridge, UK*
[18]*King's College London and Guy's and St Thomas' PET Centre,*
Division of Imaging Sciences and Biomedical Engineering, King's College London, London, UK
[19]*Department of Psychiatry, The Royal's Institute of Mental Health Research, University of Ottawa, ON, Canada*
[20]*Department of Psychoeducation and Psychology, University of Quebec in Outaouais, Gatineau, QC, Canada*
[21]*Department of Psychiatry, University of Turku and Turku University Hospital, Finland*
[22]*Institute of Neuroscience and Medicine (INM-1), Research Centre Jülich, Jülich, Germany*

Abstract

Neurotransmitter receptors support the propagation of signals in the human brain. How receptor systems are situated within macroscale neuroanatomy and how they shape emergent function remains poorly understood, and there exists no comprehensive atlas of receptors. Here we collate positron emission tomography data from >1 200 healthy individuals to construct a whole-brain 3-D normative atlas of 19 receptors and transporters across 9 different neurotransmitter systems. We find that receptor profiles align with structural connectivity and mediate function, including neurophysiological oscillatory dynamics and resting state hemodynamic functional connectivity. Using the Neurosynth cognitive atlas, we uncover a topographic gradient of overlapping receptor distributions that separates extrinsic and intrinsic psychological processes. Finally, we find both expected and novel associations between receptor distributions and cortical abnormality patterns across 13 disorders. We replicate all findings in an independently collected autoradiography dataset. This work demonstrates how chemoarchitecture shapes brain structure and function, providing a new direction for studying multi-scale brain organization.

INTRODUCTION

The brain is a complex system that integrates signals across spatial and temporal scales to support cognition and behaviour. The key neural signalling molecule is the neurotransmitter: chemical agents that relay messages across synapses. While neurotransmitters carry the message, neurotransmitter receptors act as ears that cover the cellular membrane, determining how the postsynaptic neuron will respond. By modulating the excitability and firing rate of the cell, neurotransmitter receptors effectively mediate the transfer and propagation of electrical impulses. As such, neurotransmitter receptors drive synaptic plasticity, modify neural states, and ultimately

---

* bratislav.misic@mcgill.ca

Receptor/ transporter	Neurotransmitter	Tracer	Measure	N	Age	References
D_1	dopamine	[^{11}C]SCH23390	BP_{ND}	13 (7)	33 ± 13	Kaller et al., 2017 [74]
D_2	dopamine	[^{11}C]FLB-457	BP_{ND}	37 (20)	48.4 ± 16.9	Smith et al., 2019 [134, 157]
D_2	dopamine	[^{11}C]FLB-457	BP_{ND}	55 (29)	32.5 ± 9.7	Sandiego et al., 2015 [134, 135, 154, 157, 192]
DAT*	dopamine	[^{123}I]-FP-CIT	SUVR	174 (65)	61 ± 11	Dukart et al., 2018 [37]
NET*	norepinephrine	[^{11}C]MRB	BP_{ND}	77 (27)	33.4 ± 9.2	Ding et al., 2010 [12, 24, 35, 133]
5-HT_{1A}	serotonin	[^{11}C]WAY-100635	BP_{ND}	35 (17)	26.3 ± 5.2	Savli et al., 2012 [138]
5-HT_{1B}	serotonin	[^{11}C]P943	BP_{ND}	65 (16)	33.7 ± 9.7	Gallezot et al., 2010 [10, 51, 93, 101, 102, 118, 136]
5-HT_{1B}	serotonin	[^{11}C]P943	BP_{ND}	23 (8)	28.7 ± 7.0	Savli et al., 2012 [138]
5-HT_{2A}	serotonin	[^{11}C]Cimbi-36	B_{max}	29 (14)	22.6 ± 2.7	Beliveau et al., 2017 [13]
5-HT_4	serotonin	[^{11}C]SB207145	B_{max}	59 (18)	25.9 ± 5.3	Beliveau et al., 2017 [13]
5-HT_6	serotonin	[^{11}C]GSK215083	BP_{ND}	30 (0)	36.6 ± 9.0	Radhakrishnan et al., 2018 [121, 122]
5-HTT*	serotonin	[^{11}C]DASB	B_{max}	100 (71)	25.1 ± 5.8	Beliveau et al., 2017 [13]
$\alpha_4\beta_2$	acetylcholine	[^{18}F]flubatine	V_T	30 (10)	33.5 ± 10.7	Hillmer et al., 2016 [9, 65]
M_1	acetylcholine	[^{11}C]LSN3172176	BP_{ND}	24 (11)	40.5 ± 11.7	Naganawa et al., 2021 [103]
VAChT*	acetylcholine	[^{18}F]FEOBV	SUVR	4 (1)	37 ± 10.2	PI: L Tuominen & S Guimond
VAChT*	acetylcholine	[^{18}F]FEOBV	SUVR	18 (13)	66.8 ± 6.8	Aghourian et al., 2017 [1]
VAChT*	acetylcholine	[^{18}F]FEOBV	SUVR	5 (1)	68.3 ± 3.1	Bedard et al., 2019 [11]
VAChT*	acetylcholine	[^{18}F]FEOBV	SUVR	3 (3)	66.6 ± 0.94	PI: TW Schmitz & RN Spreng
NMDA	glutamate	[^{18}F]GE-179	V_T	29 (8)	40.9 ± 12.7	Galovic et al., 2021 [53, 54, 94]
$mGluR_5$	glutamate	[^{11}C]ABP688	BP_{ND}	73 (48)	19.9 ± 3.04	Smart et al., 2019 [155]
$mGluR_5$	glutamate	[^{11}C]ABP688	BP_{ND}	22 (10)	67.9 ± 9.6	PI: P Rosa-Neto & E Kobayashi
$mGluR_5$	glutamate	[^{11}C]ABP688	BP_{ND}	28 (13)	33.1 ± 11.2	DuBois et al., 2016 [36]
$GABA_{A/BZ}$	GABA	[^{11}C]flumazenil	B_{max}	16 (9)	26.6 ± 8	Nørgaard et al., 2021 [106]
H_3	histamine	[^{11}C]GSK189254	V_T	8 (1)	31.7 ± 9.0	Gallezot et al., 2017 [52]
CB_1	cannabinoid	[^{11}C]OMAR	V_T	77 (28)	30.0 ± 8.9	Normandin et al., 2015 [39, 104, 109, 124]
MOR	opioid	[^{11}C]carfentanil	BP_{ND}	204 (72)	32.3 ± 10.8	Kantonen et al., 2020 [75]

TABLE 1. **Neurotransmitter receptors and transporters included in analyses |** BP_{ND} = non-displaceable binding potential; V_T = tracer distribution volume; B_{max} = density (pmol/ml) converted from binding potential (5-HT) or distributional volume (GABA) using autoradiography-derived densities; SUVR = standard uptake value ratio. Values in parentheses (under N) indicate number of females. Neurotransmitter receptor maps without citations refer to unpublished data. In those cases, contact information for the study PI is provided in Table S3. Table S3 also includes more extensive methodological details such as PET camera, number of males and females, modelling method, reference region, scan length, and modelling notes. Asterisks indicate transporters.

shape network-wide communication [149, 152, 174].

How spatial distributions of neurotransmitter receptors relate to brain structure and shape brain function at the system level remains unknown. Recent technological advances allow for high resolution reconstructions of the brain's wiring patterns. These wiring patterns display non-trivial architectural features including specialized network modules that support the segregation of information [160], as well as densely interconnected hub regions that are thought to support the integration of information [159, 175]. The spatial arrangement of neurotransmitter receptors on this network presumably guides the flow of information and the emergence of cognitive function. Therefore, understanding the link between structure and function is inherently incomplete without a comprehensive map of the chemoarchitecture of the brain [81, 113, 193, 195].

A primary obstacle to studying the relative density distributions of receptors across multiple neurotransmitter systems is the lack of comprehensive openly accessible datasets. An important exception is the autoradiography dataset of 15 neurotransmitter receptors and receptor binding sites, collected in three post-mortem brains [193]. However, these autoradiographs are only available in 44 cytoarchitectonically defined cortical areas. Alternatively, positron emission tomography (PET) can estimate *in vivo* receptor concentrations across the whole brain. Despite the relative ease of mapping receptor densities using PET, there are nonetheless difficulties in constructing a comprehensive PET dataset of neurotransmitter receptors. Due to the radioactivity of the injected PET tracer, mapping multiple different receptors in the same individual is not considered a safe practice. Combined with the fact that PET image acquisition is relatively expensive, cohorts of control subjects are small and typically only include one or two tracers. There-

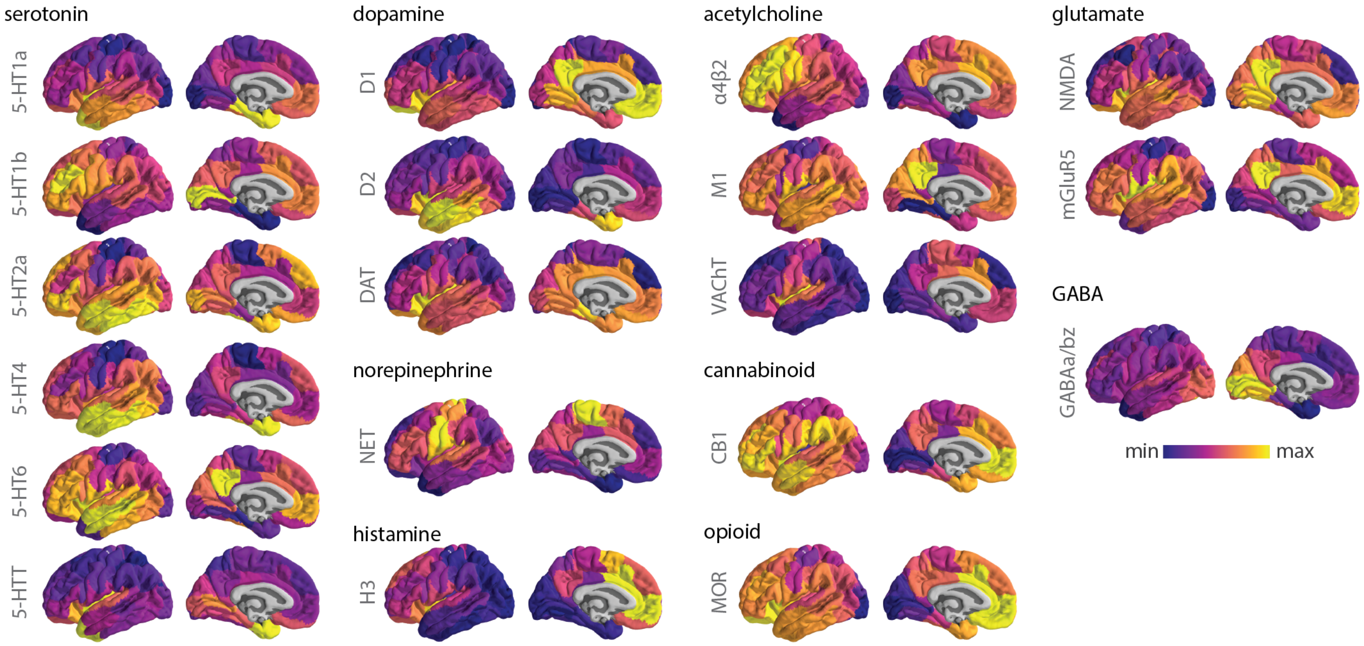

Figure 1. **PET images of neurotransmitter receptors and transporters** | PET tracer images were collated and averaged to produce mean receptor distribution maps of 19 different neurotransmitter receptors and transporters across 9 different neurotransmitter systems and a combined total of over 1 200 healthy participants.

fore, constructing a comprehensive atlas of neurotransmitter receptor densities across the brain requires extensive data sharing efforts from multiple research groups [13, 38, 80, 92, 106, 108].

Here we curate and share an atlas of PET-derived whole-brain neurotransmitter receptor maps from 19 unique neurotransmitter receptors, receptor binding sites, and transporters, across 9 different neurotransmitter systems and over 1 200 healthy individuals, available at https://github.com/netneurolab/hansen_receptors. We use multiple imaging modalities to comprehensively situate cortical neurotransmitter receptor densities within microscale and macroscale neural architectures. Using diffusion weighted MRI and functional MRI, we show that neurotransmitter receptor densities follow the organizational principles of the brain's structural and functional connectomes. Moreover, we find that neurotransmitter receptor densities shape magnetoencephalography (MEG)-derived oscillatory neural dynamics. To determine how neurotransmitter receptor distributions affect cognition and disease, we map receptor densities to meta-analytic (Neurosynth-derived) functional activations, where we uncover a spatially covarying axis of neuromodulators and mood-related processes. Next, we link receptor distributions to ENIGMA-derived patterns of cortical atrophy across 13 neurological, psychiatric, and neurodevelopmental disorders, uncovering specific receptor-disorder links. We validate our findings and extend the scope of the investigation to additional receptors using an independently collected autoradiography neurotransmitter receptor dataset [194]. Altogether we demonstrate that, across spatial and temporal scales, chemoarchitecture consistently plays a key role in brain function.

RESULTS

A comprehensive cortical profile of neurotransmitter receptor densities was constructed by collating PET images from a total of 19 different neurotransmitter receptors, transporters, and receptor binding sites, across 9 different neurotransmitter systems, including dopamine, norepinephrine, serotonin, acetylcholine, glutamate, GABA, histamine, cannabinoid, and opioid (Fig. 1). All PET images are acquired in healthy participants (see Table 1 for a complete list of receptors and transporters, corresponding PET tracers, ages, and number of participants). Each PET tracer map was processed according to the best practice for the radioligand; for detailed acquisition and processing protocols see the publications listed in Table 1. A group-average tracer map was constructed across participants within each study. To mitigate variation in image acquisition and preprocessing, and to ease biological interpretability, all PET tracer maps were parcellated into the same 100 cortical regions and z-scored [139]. Note that although the data includes both cortical and subcortical data, we restrict our analyses to the cortex. After parcellating and normalizing the data, maps from different studies of the same tracer were averaged together (Fig. S1 shows consistencies across studies). In total, we present tracer maps for 19 unique neurotrans-

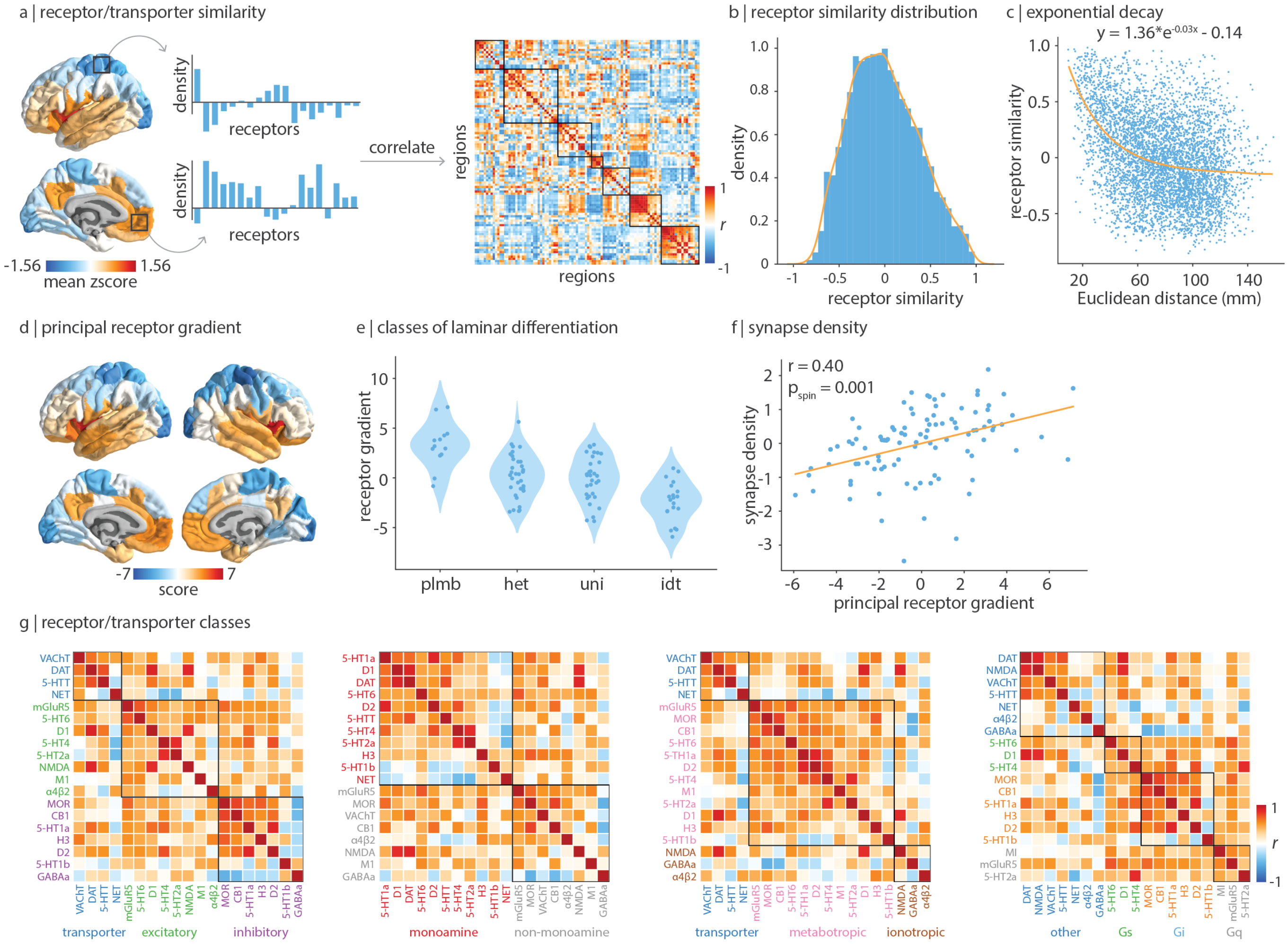

Figure 2. **Constructing a cortical neurotransmitter receptor and transporter atlas** | PET maps for 19 different neurotransmitter receptors and transporters were z-scored and collated into a single neurotransmitter receptor atlas. (a) For each pair of brain regions, the receptor density profiles are correlated (Pearson's r) to construct the receptor similarity matrix (ordered according to the Yeo-Krienen intrinsic networks: frontoparietal, default mode, dorsal attention, limbic, ventral attention, somatomotor, visual [191]). (b) Receptor similarity is approximately normally distributed. (c) Receptor similarity decays exponentially with the Euclidean distance between centroid coordinates of brain regions. (d) The first principal component of receptor density. (e) The first principal gradient of receptor density stratified by classes of laminar differentiation reveals a gradient from idiotypic regions to paralimbic regions (one-way ANOVA $F = 18.26$, $p < 0.001$; PLMB=paralimbic, HET=heteromodal, UNI=unimodal, IDT=idiotypic) [97, 116]. (f) The principal receptor gradient is significantly correlated with synapse density (measured using the synaptic vesicle glycoprotein 2A-binding [^{11}C]-UCBJ PET tracer; Pearson's $r(98) = 0.40$, $p_{\text{spin}} = 0.001$, CI $= [0.23, 0.56]$ two-tailed). (g) Pearson's correlation between pairs of receptor/transporter distributions are shown stratified by excitatory vs. inhibitory, monoamine vs. non-monoamine, ionotropic vs. metabotropic, and Gs- vs. Gi- vs. Gq-coupled metabotropic receptors.

mitter receptors and transporters from a combined total of 1238 healthy participants, resulting in a 100×19 matrix of relative neurotransmitter receptor/transporter densities. Finally, we repeat all analyses in an independently collected autoradiography dataset of 15 neurotransmitter receptors (Table S1; [194]), and across alternative brain parcellations [139].

Receptor distributions reflect structural and functional organization

To quantify the potential for two brain regions to be similarly modulated by endogenous or exogenous input, we compute the correlation of receptor/transporter fingerprints between pairs of brain regions (Fig. 2a). Hereafter, we refer to this quantity as "receptor similarity", analogous to other commonly used measures of inter-regional attribute similarity including anatomical covariance [43], morphometric similarity [146],

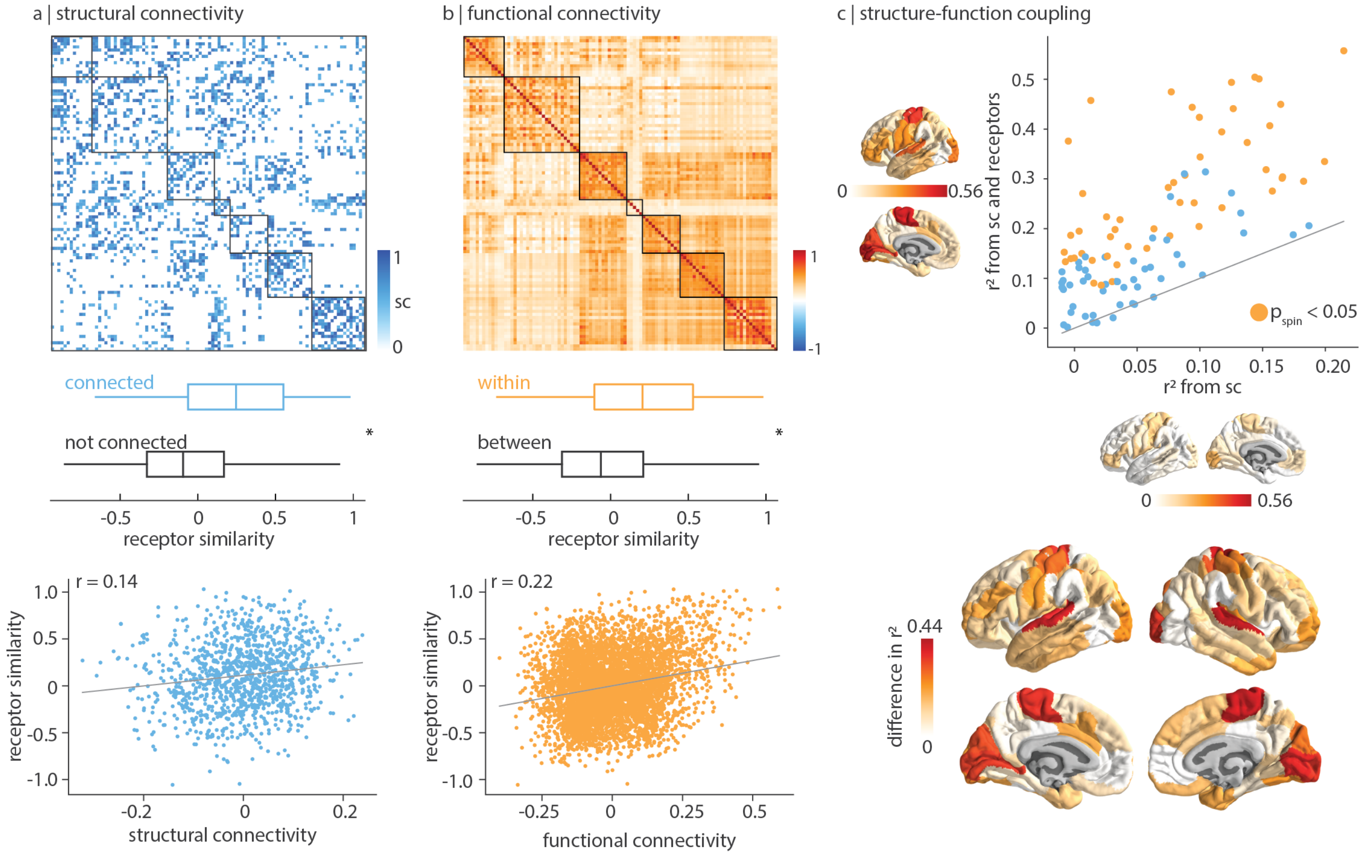

Figure 3. **Receptor distributions reflect structural and functional organization** | (a) Top: group-consensus weighted structural connectivity matrix. Middle: receptor similarity is significantly greater between regions that are physically connected, against distance- and edge length-preserving null structural connectivity matrices ($p = 0.0001$; [16]). Bottom: receptor similarity is significantly positively correlated with structural connectivity, after distance regression (Pearson's $r(1134) = 0.14$, $p < 0.001$, CI $= [0.08, 0.20]$). (b) Top: group-average functional connectivity matrix. Middle: receptor similarity is significantly greater within regions in the same functional network ($p_{\text{spin}} = 0.016$). Bottom: receptor similarity is positively correlated with functional connectivity (Pearson's $r(4948) = 0.22$, $p < 0.001$, CI $= [0.20, 0.25]$). (c) Regional structure-function coupling was computed as the fit (R^2_{adj}) between communicability of the weighted structural connectome and functional connectivity. Top: structure-function coupling at each brain region is plotted when receptor similarity is excluded (x-axis) and included (y-axis) in the model. Yellow points indicate brain regions where receptor information significantly augments structure-function coupling ($p_{\text{spin}} < 0.05$, FDR-corrected, one-sided). Bottom: the difference in adjusted R^2 when receptor similarity is and isn't included in the regression model. Asterisks in panels (a) and (b) denote significance. Boxplots in panels (a) and (b) represent the 1st, 2nd (median) and 3rd quartiles, whiskers represent the non-outlier end-points of the distribution, and diamonds represent outliers. Connectomes in panel (a) and (b) are ordered according to the Yeo-Krienen intrinsic networks (order: frontoparietal, default mode, dorsal attention, limbic, ventral attention, somatomotor, visual) [191].

gene coexpression [5, 49, 125], temporal profile similarity [148], and microstructural similarity [116]. Receptor similarity is approximately normally distributed (Fig. 2b), and decreases exponentially with Euclidean distance which supports the notion that a fundamental feature of the brain is its spatial autocorrelation (Fig. 2c; [14, 49, 68, 128, 132, 148, 153, 168]). We confirm that no single receptor or transporter exerts undue influence on the receptor similarity matrix (see *Sensitivity and robustness analyses*).

Receptor similarity addresses the between-region similarity of receptor fingerprints. To complement this, we calculated the first principal component of receptor density which represents a regional quantification of receptor similarity (Fig. 2d). This gradient separates insular and cingulate cortex from somatomotor and posterior parietal regions, and resembles the macaque principal receptor expression gradient [48]. The first principal component differentiates laminar classes, supporting the notion that receptor expression strongly depends on lamination (Fig. 2e, one-way ANOVA $F = 18.26$, $p < 0.001$; [97, 114, 115]). Additionally, we find a significant correlation between the receptor gradient and synapse density, consistent with the finding that the macaque receptor gradient increases with the number of dendritic spines (Fig. 2f; Pearson's $r(98) = 0.40$, $p_{\text{spin}} =$

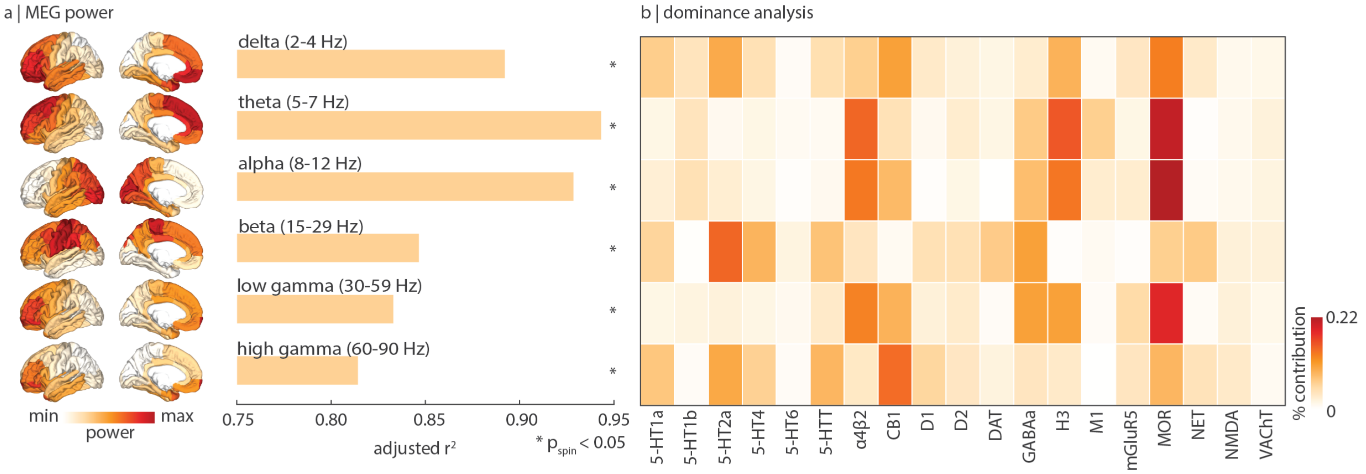

Figure 4. **Receptor profiles shape oscillatory neural dynamics** | We fit a multilinear regression model that predicts MEG-derived power distributions from receptor distributions. (a) Receptor distributions closely correspond to all six MEG-derived power bands ($0.81 \leq R^2_{\text{adj}} \leq 0.94$). The significance of each model is assessed against a spatial-permutation preserving null model, and corrected for multiple comparisons (FDR-correction). Asterisks denote significant models (FDR-corrected $p_{\text{spin}} < 0.05$, one-tailed). (b) Dominance analysis distributes the fit of the model across input variables such that the contribution of each variable can be assessed and compared to other input variables. The percent contribution of each input variable is defined as the variable's dominance normalized by the total fit (R^2_{adj}) of the model.

0.001, CI $= [0.23, 0.56]$, two-tailed) [48]. For completeness, we stratify receptors by biological mechanisms (excitatory/inhibitory, ionotropic/metabotropic, Gs/Gi/Gq-coupled metabotropic pathways) and neurotransmitter protein structure (monoamine/non-monoamine), to provide additional insight about the underlying biological pathways (Fig. 2g).

Using group-consensus structural and resting-state functional connectomes from 326 unrelated individuals (see *Methods* for details), we show that neurotransmitter receptor organization reflects structural and functional connectivity. Specifically, we find that receptor similarity is greater between pairs of brain regions that are structurally connected, suggesting that anatomically connected areas are likely to be co-modulated (Fig. 3a). To ensure the observed relationship between structural connections and receptor similarity is not due to spatial proximity or network topography, we assessed significance against density-, degree- and edge length-preserving surrogate structural connectivity matrices ($p = 0.0001$, $10\,000$ repetitions [16]). Additionally, we find that receptor similarity is significantly correlated with structural connectivity, after regression Euclidean distance from both modalities (Pearson's $r(1134) = 14$, $p < 0.001$, CI $= [0.08, 0.20]$).

Likewise, receptor similarity is significantly greater between brain regions that are within the same intrinsic networks than between different intrinsic networks, according to the Yeo-Krienen 7-network classification ($p_{\text{spin}} = 0.016$, $10\,000$ repetitions, Fig. 3b [191]). This suggests that areas that are in the same cognitive system tend to have similar receptor profiles [193]. Significance was assessed non-parametrically by permuting the intrinsic network affiliations while preserving spatial autocorrelation ("spin test"; [3, 91]). We also find that receptor similarity is significantly correlated with functional connectivity, after regressing Euclidean distance from both matrices (Pearson's $r(4948) = 0.22$, $p < 0.001$, CI $= [0.20, 0.25]$). In other words, we observe that brain regions with similar receptor and transporter composition show greater functional co-activation. Collectively, these results demonstrate that receptor profiles are systematically aligned with patterns of structural and functional connectivity above and beyond spatial proximity, consistent with the notion that receptor profiles guide inter-regional signaling.

Since neurotransmitter receptor and transporter distributions are organized according to structural and functional architectures, we next asked whether receptor/transporter distributions might augment the coupling between brain structure and function. To quantify structure-function coupling, we relied on the communicability of the weighted structural connectome, defined as the weighted average of all walks and paths between two brain regions (but see results using alternative methods in Fig. S2). Communicability represents a form of decentralized diffusive communication on the structural connectome [26], and has been previously shown to mediate the link between brain structure and function [41, 60, 144]. Structure-function coupling at every brain region is defined as the adjusted R^2 of a simple linear regression model that fits regional communicability (i.e. the communicability between a brain region to every other brain region) to regional functional connectivity (i.e. the functional connectivity between a brain region and every other brain region). We then included regional receptor similarity as an independent variable, to assess how receptor information changes structure-function coupling. Significance was assessed against a null distribution of adjusted R^2 from a model that adds a rotated regional receptor similarity vector (10 000 repetitions, one-sided). Next, we cross-validated each regression model using a distance-dependent method that was previously developed in-house (Fig. S4; see *Methods* for details [61]). We find that including receptor profiles as an input variable alongside brain structure significantly improves the prediction of regional functional connectivity in unimodal areas and the paracentral lobule (Fig. 3c).

Receptor profiles shape oscillatory neural dynamics

Given that neurotransmitter receptors modulate the firing rates of neurons and therefore population activity, we sought to relate the cortical patterning of neurotransmitter receptors to neural oscillations [151]. We used MEG power spectra across six canonical frequency bands from 33 unrelated participants in the Human Connectome Project (see *Methods* for details; [57, 147, 177]). We fit a multiple linear regression model that predicts the cortical power distribution of each frequency band from neurotransmitter receptor and transporter densities. We then cross-validated the model using a distance-dependent method (Fig. S5; see *Methods* for details). In addition to the cross-validation, we assess the significance of each model against a spin-permuted null model (10 000 repetitions) and find that all models are significant after FDR-correction ($p_{\text{spin}} < 0.05$, one-sided) [15]. We find a close fit between receptor densities and MEG-derived power ($0.81 \leq R^2_{\text{adj}} \leq 0.94$; Fig. 4a), suggesting that overlapping spatial topographies of multiple neurotransmitter systems may ultimately manifest as coherent oscillatory patterns.

To identify independent variables (receptors/transporters) that contribute most to the fit, we applied dominance analysis, a technique that assigns a proportion of the final R^2_{adj} to each independent variable [7]. Dominance was normalized by the total fit of the model (R^2_{adj}), such that dominance is comparable across models (Fig. 4b). We find that, compared to other receptors, the spatial distribution of MOR (opioid), H_3 (histamine), and $\alpha_4\beta_2$ make a large contribution to the fit between receptors and lower-frequency (theta, alpha) power bands [117, 119, 186, 189, 198]. Interestingly, we find that faster frequency bands (beta, low gamma) are linked with fast-acting ionotropic receptors such as $\alpha_4\beta_2$ and GABA_A, although we note that the ionotropic NMDA receptor makes little contribution across all frequency bands. The prominence of ionotropic receptors is also observed in the autoradiography dataset (see *Replication using autoradiography* and Fig. S6). Additionally, when we stratify dominance by receptor classes, we find that inhibitory, non-monoamine, and Gi-coupled receptors are more dominant than excitatory, monoamine, and Gs-coupled receptors, respectively (Fig. S3a).

Mapping receptors to cognitive function

Previously, we showed that receptor and transporter distributions follow the structural and functional organization of the brain, and that receptors are closely linked to neural dynamics. In this and the next subsections, we investigate how the spatial distribution of neurotransmitter receptors and transporters correspond to cognitive processes and disease vulnerability.

We used Neurosynth to derive meta-analytic task activation maps, which represent the probability that specific brain regions are activated during multiple cognitive tasks [190]. We selected a subset of 123 cognitive processes at the intersection of Neurosynth and the Cognitive Atlas [61, 120], and parcellated the data into the same 100-region atlas used for receptor maps, resulting in a region × cognitive process matrix of functional activations. We then applied partial least squares (PLS) analysis to identify a multivariate mapping between neurotransmitter receptors/transporters and functional activation maps (see *Methods* for details and Table S2 for the complete list of 123 cognitive terms; [82, 95]).

PLS analysis extracted a significant latent variable relating receptor/transporter densities to functional activation across the brain ($p_{\text{spin}} = 0.010$, one-tailed). The latent variable represents the dominant spatial pattern of receptor distributions (receptor weights) and functional activations (cognitive weights) that together capture 56% of the covariance between the two datasets (Fig. 5a). Projecting the receptor density (functional activation) matrix back onto the receptor (cognitive) weights reflects how well a brain area exhibits the receptor and cognitive weighted pattern, which we refer to as “receptor scores” and “cognitive scores”, respectively (Fig. 5b, c). The receptor and cognitive score patterns reveal a sensory-fugal spatial gradient, separating limbic, paralimbic, and insular cortices from visual and somatosensory cortices. We then cross-validated the correlation between receptor and cognitive scores using a distance-dependent method (Fig. 5d, mean out-of-sample Pearson’s $r(98) = 0.60$, $p_{\text{spin}} = 0.03$, one-sided; see *Methods* for details on the cross-validation). This result demonstrates a link between receptor distributions and cognitive specialization that is perhaps mediated by laminar differentiation and synaptic hierarchies.

To identify the receptors and cognitive processes that contribute most to the spatial pattern in Fig. 5b and c, we correlated each variable with the score pattern (Fig. 5e–f; for all stable term loadings, see Fig. S7). This results in a “loading” for each receptor and cognitive process, where positively loaded receptors covary with positively loaded

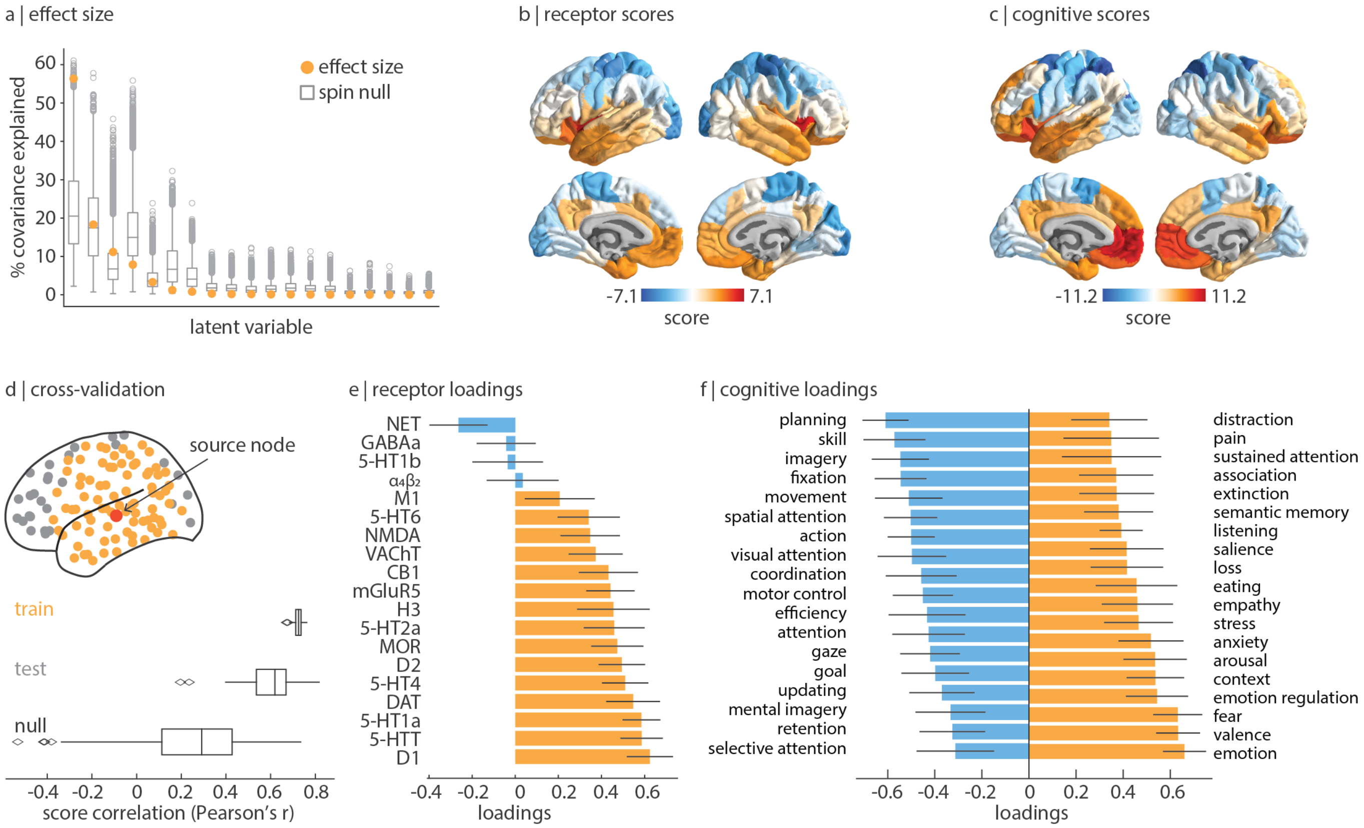

Figure 5. **Mapping receptors to cognitive function** | (a) Using partial least squares analysis (PLS), we find a significant latent variable that accounts for 56% of the covariation between receptor distributions and Neurosynth-derived cognitive functional activation ($p_{\text{spin}} = 0.010$, 10 000 repetitions, one-sided). (b)–(c) This latent variable represents a pattern of coactivation between receptors ("receptor scores") and cognitive terms ("cognitive scores"). (d) The PLS model was cross-validated using a method that stratifies the training (yellow points) and test set (grey points) based on the distance between each node to a source node (red point), and the procedure is repeated such that each brain region is assigned as the source node once (100 repetitions). The significance of the mean out-of-sample test-set correlation was assessed against a null distribution of mean correlation constructed by rotating the receptor density matrix prior to the PLS analysis (see *Methods* for details). (e) Receptor loadings are computed as the correlation (Pearson's r) between each receptor's distribution across the cortex and the PLS-derived scores, and can be interpreted as the contribution of each receptor to the latent variable. (f) Similarly, cognitive loadings are computed as the correlation (Pearson's r) between each term's functional activation across brain regions and the PLS-derived scores, and can be interpreted as the cognitive processes that contribute most to the latent variable. Here, only the 25% most positively and negatively loaded cognitive processes are shown. For all stable cognitive loadings, see Fig. S7 and for all 123 cognitive processes included in the analysis, see Table S2. 95% confidence intervals are estimated for receptor and cognitive loadings using bootstrap resampling (10 000 repetitions).

cognitive processes in positively scored brain regions, and vice versa for negative loadings. Interestingly, we find that almost all receptors/transporters have positive loading, with metabotropic serotonergic and dopaminergic receptors having the greatest loadings (Fig. 5e, Fig. S3b). The cognitive processes with large positive loadings are enriched for emotional and affective processes such as "emotion", "valence", and "fear". This suggests that the combination of serotonergic and dopaminergic receptor distributions covary with mood-related functional activation in insular and limbic regions, consistent with the role of serotonin and dopamine neurotransmitter systems in mood processing and mood disorders [129, 173]. On the other hand, we find that only NET has stable negative loading, and that it spatially covaries with functions such as "planning", "skill", and "fixation" in primarily unimodal regions. This is consistent with the notion that norepinephrine systems are involved in integrative functions that require coordination across segregated brain regions [127, 149, 150]. Collectively, these results demonstrate a direct link between cortex-wide molecular receptor distributions and functional specialization.

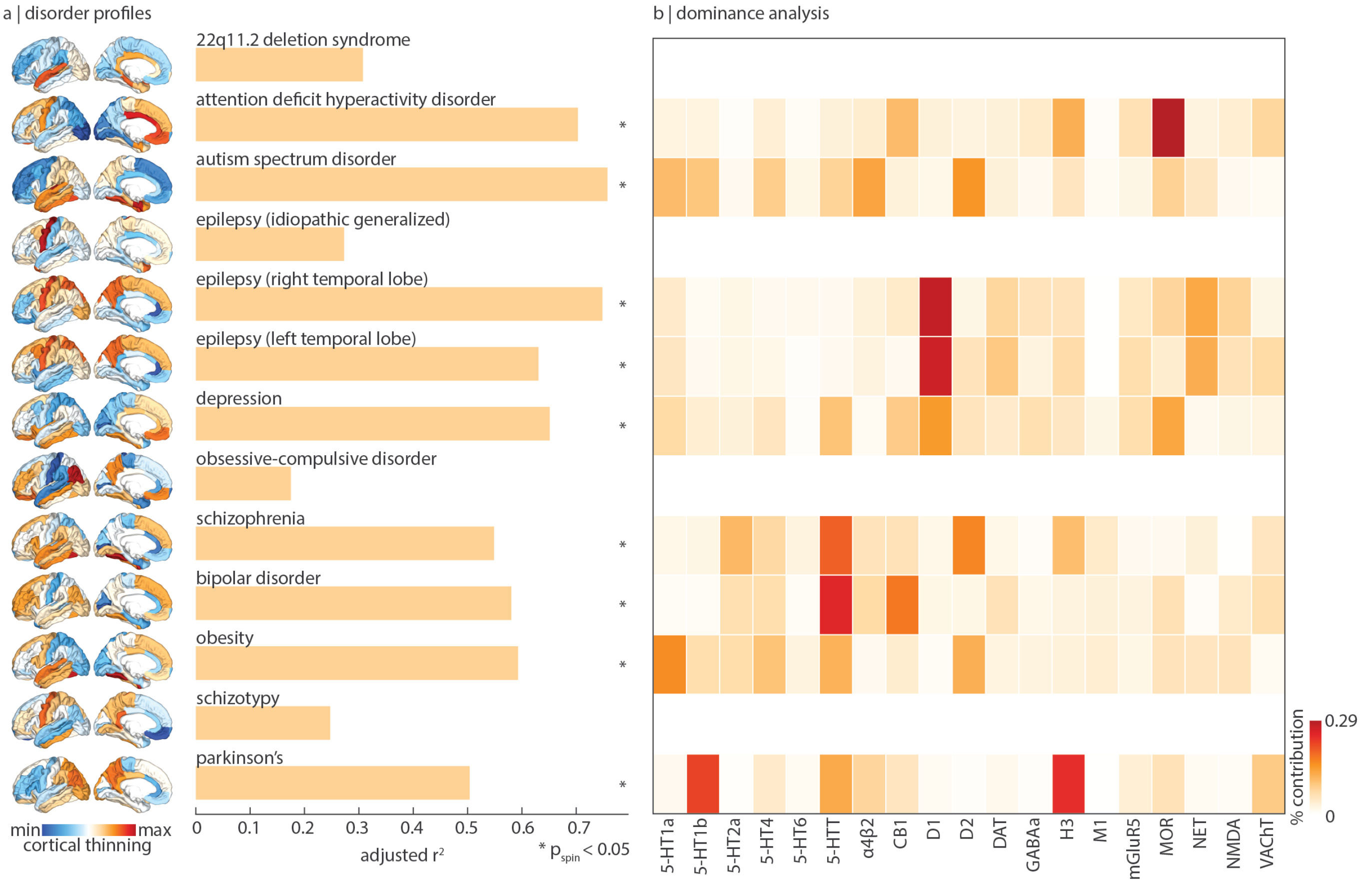

Figure 6. **Mapping receptors to disease vulnerability** | Using a multilinear model, neurotransmitter receptor/transporter distributions were fit to patterns of cortical abnormality for thirteen neurological, psychiatric, and neurodevelopmental disorders, collected by the ENIGMA consortium [85, 169]. (a) The significance of each model is assessed using a spatial autocorrelation preserving null model and is corrected for multiple comparisons (FDR). Asterisks denote significant models (FDR-corrected $p_{\text{spin}} < 0.05$, one-sided [15]). (b) Dominance analysis distributes the fit of the model across input variables such that the contribution of each variable can be assessed and compared to other input variables. The percent contribution of each input variable is defined as the variable's dominance normalized by the total fit (R^2_{adj}) of the model. Note that dominance analysis is not applied to the input variables of non-significant models (i.e. 22q deletion syndrome, idiopathic generalized epilepsy, OCD, schizotypy), and that this analysis is conducted using the Desikan-Killiany atlas because this is the only representation of ENIGMA datasets [33].

Mapping receptors and transporters to disease vulnerability

Neurotransmitter receptors and transporters are implicated in multiple diseases and disorders. Identifying the neurotransmitter receptors/transporters that correspond to specific disorders is important for developing new therapeutic drugs. We therefore sought to relate neurotransmitter receptors and transporters to patterns of cortical abnormality across a range of neurological, developmental, and psychiatric disorders. We used datasets from the ENIGMA consortium for a total of 13 disorders including: 22q11.2 deletion syndrome (22q) [165], attention deficit hyperactivity disorder (ADHD) [67], autism spectrum disorder (ASD) [179], idiopathic generalized epilepsy, right and left temporal lobe epilepsy [188], depression [140], obsessive-compulsive disorder (OCD) [19], schizophrenia [176], bipolar disorder (BD) [64], obesity [111], schizotypy [79], and Parkinson's disease (PD) [83]. While most disorders show decreases in cortical thickness, some (e.g. 22q, ASD, schizotypy) also show regional increases in cortical thickness. We therefore refer to the disorder profiles as "cortical abnormalities". All cortical abnormality maps were collected from adult patients, following identical processing protocols, for a total of over 21 000 scanned patients against almost 26 000 controls. We then fit a multiple regression model that predicts each disorder's cortical abnormality pattern from receptor and transporter distributions (Fig. 6). We assessed the significance of each model fit against an FDR-corrected one-sided spatial-autocorrelation preserving null model, and evaluated each model using distance-dependent cross-validation (Fig. S8; see *Methods* for details on the cross-validation).

Figure 6a shows how receptor distributions map onto cortical abnormaltiy patterns across multiple disorders. We find that some disorders are more heavily influenced by receptor distribution than others ($0.17 < R^2_{\text{adj}} < 0.76$). 22q deletion syndrome, idiopathic generalized epilepsy, OCD, and schizotypy show low and non-significant correspondence with receptor distributions, whereas ADHD, autism, and temporal lobe epilepsies show greater correspondence with receptor distributions. The dominance analysis in Figure 6b shows the contribution of each input variable to the fit of the model, normalized by the total fit (adjusted R^2). Interestingly, we find that serotonin transporter (5-HTT) distributions contribute more to schizophrenia and bipolar disorder disorder profiles than any other receptors. Furthermore, the mu-opioid receptor is the strongest contributor of ADHD cortical abnormalities, consistent with findings from animal models [29, 130], and three of the four greatest contributors to the obesity cortical profile are serotonergic [178]. We also note that in some cases the analyses do not necessarily recover the expected relationships. For instance, in PD, the dopamine receptors are not implicated, likely because the analysis was restricted to cortex only. Additionally, serotonin receptors do not make large contributions to depression, possibly because changes in cortical thickness does not directly measure the primary pathophysiology associated with some brain diseases. Although this analysis points to mappings between receptors and disorder profiles, we find no significant differential contribution of receptor classes to disorder profiles (Fig. S3c). Our results present an initial step towards a comprehensive "look-up table" that relates neurotransmitter systems to multiple brain disorders.

Replication using autoradiography

In the present report, we comprehensively situate neurotransmitter receptor and transporter densities within the brain's structural and functional architecture. However, estimates for neurotransmitter receptor densities are acquired from PET imaging alone, and the way in which densities are quantified varies across radioligands, image acquisition protocols, and preprocessing. Autoradiography is an alternative technique to measure receptor density, and captures local densities at a defined number of post-mortem brain sections [196]. Due to the high cost and labor intensity of acquiring autoradiographs, there does not yet exist a complete autoradiography 3-D cross-cortex atlas of receptors (but see Funck et al. [50]).

Nonetheless, we repeated the analyses in an autoradiography dataset of 15 neurotransmitter receptors across 44 cytoarchitectonically defined cortical areas, from three post-mortem brains [59, 194]. This set of 15 neurotransmitter receptors consists of a diverse set of ionotropic and metabotropic receptors, including excitatory glutamate, acetylcholine, and norepinephrine receptors (see Table S1 for a complete list of receptors). Importantly, eight of the fifteen receptors in the autoradiography dataset are not included in the PET dataset, which precludes direct comparisons between the two datasets. Receptor similarity is shown in Fig. S9a. Despite the alternate set of neurotransmitter receptors, we find that autoradiography-derived receptor similarity is significantly correlated with PET-derived receptor similarity (Pearson's $r(1033) = 0.38$, $p < 0.001$, CI $= [0.33, 0.43]$; Fig. S9a), and decays exponentially with Euclidean distance. Additionally, autoradiography- and PET-derived receptor gradients are correlated (Pearson's $r(44) = 0.50$, $p_{\text{perm}} = 0.0004$, CI $= [0.25, 0.69]$, two-sided). Next, we find that autoradiography-derived receptor densities follow similar architectural patterns as the PET-derived receptor densities. Receptor similarity is non-significantly greater between structurally connected brain regions ($p = 0.19$), and significantly correlated with structural connectivity (Pearson's $r(329) = 0.39$, $p < 0.001$, CI $= [0.30, 0.48]$; Fig. S9d). It is also significantly greater in regions within the same intrinsic network ($p_{\text{spin}} = 0.03$), and is significantly correlated with functional connectivity (Pearson's $r(1033) = 0.21$, $p < 0.001$, CI $= [0.16, 0.28]$; Fig. S9e). As before, receptor information augments structure-function coupling in visual, paracentral, and somatomotor regions (Fig. S9f). Finally, we show correlations of receptor density distribution between every pair of receptors in Fig. S9g.

Since the autoradiography dataset has a more diverse set of ionotropic and metabotropic receptors, we also asked whether we could replicate the dominance of ionotropic receptors for MEG oscillations. When we fit the fifteen autoradiography neurotransmitter receptors to MEG power, we find that AMPA, NMDA, GABA$_\text{A}$, and $\alpha_4\beta_2$—all ionotropic receptors—are most dominant (Fig. S6). This confirms that the fast oscillatory dynamics captured by MEG are closely related to the fluctuations in neural activity modulated by ionotropic neurotransmitter receptors.

Finally, we repeat analyses mapping receptor densities to cognitive functional activation and disease vulnerability. We find a similar topographic gradient linking autoradiography-derived receptor densities to Neurosynth-derived functional activations (Fig. S10a). Indeed, PET- and autoradiography-derived receptor and cognitive scores are correlated (Fig. S9b; Pearson's $r = -0.49$, $p_{\text{perm}} = 0.0004$, CI $= [-0.68, -0.23]$ for receptor scores; Pearson's $r = -0.75$, $p_{\text{perm}} = 0.0003$, CI $= [-0.85, -0.59]$ for cognitive scores). We also find consistencies regarding the loadings of receptors (Fig. S10c) and cognitive processes (Fig. S10d). Next, when we map autoradiography-derived receptor densities to cortical abnormality patterns of multiple disorders, we find prominent associations with receptors that were not included in the PET dataset, including a relationship between the ionotropic glutamate receptor kainate and depression (Fig. S11; [88]).

Sensitivity and robustness analyses

Finally, to ensure results are not influenced by specific methodological choices, we repeated analyses using different parcellation resolutions, different receptor subsets, and we compared alternative PET tracers to the chosen PET tracers in the present report. Due to the low spatial resolution of PET tracer binding, we opted to present our main results using a coarse resolution of 100 cortical regions [139]. However, when using a parcellation resolution of 200 and 400 cortical regions [139], we find that the mean receptor density and receptor similarity remains consistent (Fig. S12). We next asked whether any single receptor or transporter disproportionately influences receptor similarity. To test this, we iteratively removed a single receptor/transporter from the dataset and recomputed the receptor similarity matrix. These 19 different receptor similarity matrices are all highly correlated with the original similarity matrix (Pearson's $r(4948) > 0.97$), confirming that the correspondence between regional receptor profiles is not driven by a single neurotransmitter receptor/transporter.

Constructing a harmonized set of PET neurotransmitter receptor maps necessitated several methodological decisions. We combined PET maps from different research groups that used the same tracer, except for data from the Neurobiology Research Unit in Copenhagen (including [13] and [106]; see https://xtra.nru.dk/) because these images were converted from quantitative PET Units to units of density (pmol/mL) using autoradiography data. We combined two P943 ($5HT1_B$ [38, 51, 138]), two FLB457 (D_2 [134, 157]), three ABP688 ($mGluR_5$ [36, 155]), and four FEOBV (VAChT [1, 11]) tracer maps separately, all of which were highly correlated within tracer groups (Fig. S1a). Next, when multiple tracers were available for the same receptor or transporter, we opted for maps constructed from a larger number of participants (Fig. S1b; see *Methods* for details).

Finally, we tested whether participant age affects the reported results. However, only mean age of individuals included in each tracer map was available. Therefore, we fit a linear model between the mean age of scanned participants contributing to each receptor/transporter tracer map and the z-scored receptor/transporter density, for each brain region separately. We then subtracted the relationship with age from the original receptor densities, resulting in an age-regressed receptor density matrix. We find that both age-regressed receptor density and age-regressed receptor similarity is highly correlated with the original receptor density/similarity (Pearson's $r(4948) = 0.79$, $p < 0.001$, CI $= [0.77, 0.80]$ and Pearson's $r(4948) = 0.97$, $p < 0.001$, CI $= [0.97, 0.98]$ respectively; Fig. S13), suggesting that age has negligible effect on the reported findings. However, we note that this analysis is not sensitive to individual subject variability and that certain neurotransmitter receptor systems show changes in receptor availability with age [27, 76, 143].

DISCUSSION

In the present report, we curate a comprehensive 3-D atlas of 19 neurotransmitter receptors and transporters. We demonstrate that chemoarchitecture is a key layer of the multi-scale organization of the brain. Neurotransmitter receptor profiles closely align with the structural connectivity of the brain and mediate its link with function, including neurophysiological oscillatory dynamics, and resting state hemodynamic functional connectivity. The overlapping topographic distributions of these receptors ultimately manifest as patterns of cognitive specialization and disease vulnerability.

A key question in neuroscience remains how the brain's structural architecture gives rise to its function [6, 163]. The relationship between whole-brain structure and function has been viewed through the lens of "connectomics", in which the brain's structural or functional architectures are represented by regional nodes interconnected by structural and functional links. The key assumption of this model is that nodes are homogenous, effectively abstracting away important microarchitectural differences between regions. The present work is part of an emerging effort to annotate the connectome with molecular, cellular, and laminar attributes [183]. Indeed, recent work has incorporated microarray gene transcription [21, 61], cell types [4, 145], myelination [31, 32, 69], laminar differentiation [185], and intrinsic dynamics [55, 89, 100, 148] into structural and functional models of the brain.

Neurotransmitter receptors and transporters are an important molecular annotation for bridging brain structure to brain function. Neurotransmitter receptors support signal propagation across electrochemical synapses and tune neural gain [149, 152]. Despite their importance, a comprehensive cortical map of neurotransmitter receptors has remained elusive due to numerous methodological and data sharing challenges (but see the ongoing PET-BIDS effort as well as the OpenNeuro PET initiative at https://openneuropet.github.io/ [80, 108]). The present study is an ongoing Open Science grassroots effort to assemble harmonized high-resolution normative images of receptors and transporters that can be used to annotate connectomic models of the brain. This work builds on previous initiatives to map receptor densities using autoradiography, which has discovered prominent gradients of receptor expression in both human and macaque brains [48, 59, 194]. Importantly, we find consistent results between autoradiography and PET datasets, which is encouraging because the PET dataset consists of a different group of receptors and transporters, and has the added advantage of providing *in vivo* whole-brain data in large samples of healthy young participants.

We find that structurally connected areas have more similar receptor profiles, suggesting that neurotransmitter receptors are systematically aligned with network structure to regulate inter-regional communication. Indeed, we find a prominent link between receptor distribution and function, including correlated receptor similarity and functional connectivity, as well as greater receptor similarity within intrinsic functional networks. These results support the idea that the emergent functional architecture strongly depends on the underlying chemoarchitecture [151, 193]. Interestingly, we find that the canonical electrophysiological frequency bands can be captured by the overlapping topographies of multiple receptors, consistent with the notion that receptors influence function by tuning gain and synchrony between neuronal populations.

Since receptors are correlated with multiple features of brain structure and function, a natural next question is how receptor distributions relate to psychological processes. We find a spatial gradient of receptor profiles that separates limbic and insular areas from somatosensory and visual regions. This gradient represents a pattern of covariation between subsets of receptors and cognitive activations. Interestingly, although individual receptors have been associated with specific functions (i.e. D1 and selective attention [110]), our findings suggest that the combined spatial distribution of serotonergic and dopaminergic receptors underlie patterns of cognitive activation related to affect. Altogether these results offer clues about how multiple neurotransmitter systems collectively influence cognitive functions, and present novel hypotheses that future causal studies can test.

Finally, we discover a robust spatial concordance between multiple receptor maps and cortical abnormality profiles across a wide range of brain disorders. A key step toward developing therapies for specific syndromes is to reliably map them onto underlying neural systems. This goal is challenging because psychiatric and neurological nosology is built around clinical features, rather than neurobiological mechanisms [71]. Our results complement some previously established associations between disorders and neurotransmitter systems, and also reveal new associations. For instance, we find that the serotonin transporter is the strongest contributor to schizophrenia and bipolar disorder, and the third strongest contributor to depression, consistent with the fact that mood disorders are often accompanied with abnormal serotonin signaling [77, 162]. Additionally, we find that serotonin receptors are associated with obesity, consistent with the notion that serotonin systems regulate homeostatic and hedonic circuitry and are therefore implicated in food intake [178]. On the other hand, we find associations that have some preliminary support in the literature, but to our knowledge have not been conclusively established and adopted into clinical practice, including histamine H_3 in Parkinson's disease [126, 142], MOR in ADHD [29, 130], and D_1 and NET in temporal lobe epilepsy [25, 56, 161]. Mapping disease phenotypes to receptor profiles will help to identify novel targets for pharmacotherapy [78]. This analysis is restricted to a single perspective of disease pathology (cortical thinning/thickening) and should be expanded in future work to encompass other forms of disease presentation as well as the effects of age and pathology on receptor/transporter density.

Collectively, the main results in the present report aim to go beyond traditional one-to-one (i.e. univariate) associations between receptors and brain function, toward considering how multiple neurotransmitter systems work together. The present report builds on the theories generated by previous neurochemical and pharmacological causal studies, and it is encouraging to see consistent results at the level of the whole-brain, across multiple neurotransmitter systems, and using different imaging modalities. Furthermore, the comprehensive approach of this study showcases novel associations that may not have been considered before. This large-scale characterization of receptor systems should be validated in, and will hopefully inspire, future causal studies, driving the cycle of discovery. Altogether, our data and analyses provide a framework that allows us to test predictions from the wider literature and consolidate knowledge about neurotransmitter systems.

The PET receptor dataset that is presented here averages individual scans together into a single average map of receptor densities, which is intended to be representative of the healthy population. However, due to this averaging, the effect of age and sex are not thoroughly analyzed. How receptor architecture changes in healthy aging and across sexes remains an outstanding question, often limited by small sample sizes and the lack of longitudinal data (but see Nordin et al. [105] for an exciting prospective longitudinal dopamine study). Nonetheless, previously published literature has reported greater whole-brain glutamate receptor densities in men [155], greater kappa-opioid receptor density in men [184], and greater mu-opioid receptor density in women [197]. Likewise, dopamine D1 and D2 receptor availability is commonly acknowledged to decrease with age in the subcortex [70, 143], serotonin transporters and receptors have been reported to be significantly lower in older adults [76], and $GABA_A$ density is reported to be higher in older adults [27]. Future research is necessary to comprehensively disentangle the relationship between receptor expression, age, and sex.

An important future direction for studying how neurotransmitter systems comprehensively map onto brain structure and function is to focus on subcortical receptor densities. Although the 19-receptor/transporter density dataset includes subcortical volumes, the present analyses were restricted to the cortex. This was motivated by the lower signal-to-noise ratio and data reliability in subcortex across multiple imaging modalities (e.g. MEG [8, 47]) as well as lack of available data in other modalities (e.g. autoradiography [194]). Conducting a separate subcortical analysis would complement the present cortical perspective of chemoarchitecture. Indeed, multiple neurotransmitter projection systems originate in the subcortex [149] and neurodegenerative disease progression has been linked with abnormal subcortical receptor expression [87, 164]. Ultimately, characterizing heterogeneous subcortical receptor distributions is an exciting frontier for future research.

The present work should be considered alongside some important methodological considerations. First, main analyses were conducted using PET images, which detect tracer uptake at a low spatial resolution and without laminar specificity. Although results were replicated using an autoradiography dataset, and in a finer parcellation resolution, a comprehensive atlas of laminar-resolved receptor density measurements is necessary to fully understand how regional variations in receptor densities affect brain structure and function [115]. Second, PET tracer maps were acquired around the world, in different participants, on different scanners, and using specific image acquisition and processing protocols recommended for each individual radioligand [107, 182]. To mitigate this challenge, we normalized the spatial distributions and focused only on analyses related to the relative spatial topographies of receptors as opposed to the absolute values. Third, the linear models used in the present analyses assume independence between observations and linear relationships between receptors [40]; we therefore employ spatial-autocorrelation preserving null models to account for the spatial dependencies between regions throughout the report. Fourth, analyses were restricted to the cortex, obscuring the contributions of subcortical neuromodulatory systems. Fifth, although we repeat our analyses in an autoradiography dataset, eight of the fifteen receptors included in the autoradiography dataset are not included in the PET datasets and therefore a direct comparison between datasets was not possible. Altogether, a 3-D whole-brain comprehensive neurotransmitter receptor density dataset constructed using autoradiographs would be a valuable complement to the present work [50, 115, 194].

In summary, we assemble a normative 3-D atlas of neurotransmitter receptors in the human brain. We systematically map receptors to connectivity, dynamics, cognitive specialization, and disease vulnerability. Our work uncovers a fundamental organizational feature of the brain and provides new direction for a multi-scale systems-level understanding of brain structure and function.

METHODS

All code and data used to perform the analyses can be found at https://github.com/netneurolab/hansen_receptors. Volumetric PET images are included in `neuromaps` (https://github.com/netneurolab/neuromaps) where they can be easily converted between template spaces [90].

PET data acquisition

Volumetric PET images were collected for 19 different neurotransmitter receptors and transporters across multiple studies. To protect patient confidentiality, individual participant maps were averaged within studies before being shared. Details of each study, the associated receptor/transporter, tracer, number of healthy participants, age, and reference with full methodological details can be found in Table 1. A more extensive table can be found in the supplementary material (Table S3) which additionally includes the PET camera, number of males and females, PET modelling method, reference region, scan length, modelling notes, and additional references, if applicable. Note that three tracer maps were shared prior to publication, but contact information is available for the corresponding authors (Table S3). In all cases, only healthy participants were scanned ($N = 1238$, 718 males, 520 females). Images were acquired using best practice imaging protocols recommended for each radioligand [107]. Altogether, the images are an estimate proportional to receptor densities and we therefore refer to the measured value (i.e. binding potential, tracer distribution volume) simply as density. Note that the NMDA receptor tracer ([^{18}F]GE-179) binds to open (i.e. active) NMDA receptors [94, 141]. PET images were all registered to the MNI-ICBM 152 nonlinear 2009 (version c, asymmetric) template, then parcellated to 100, 200, and 400 regions according to the Schaefer atlas [139]. Receptors and transporters with more than one mean image of the same tracer (i.e. 5-HT$_{1B}$, D$_2$, mGluR$_5$, and VAChT) were combined using a weighted average. Finally, each tracer map corresponding to each receptor/transporter was z-scored across regions and concatenated into a final region by receptor matrix of relative densities.

In some cases, more than one tracer map was available for the same neurotransmitter receptor/transporter. We show the comparisons between tracers in Fig. S1b for the following neurotransmitter receptors/transporters: 5-HT1$_A$ [13, 138], 5-HT1$_B$ [13, 51, 138], 5-HT2$_A$ [13, 138, 167], 5-HTT [13, 138], CB$_1$ [86, 109], D$_2$ [2, 72, 134, 157], DAT [37, 137], GABA$_A$ [37, 106], MOR [75, 172], and NET [35, 63]. Here we make some specific notes: (1) 5-HTT and GABA$_A$ involve comparisons between the same tracers (DASB and flumazenil, respectively) but one map is converted to density using autoradiography data (see [13] and [106]) and the other is not [37, 38, 138]; (2) raclopride is a popular D$_2$ tracer but has unreliable binding in the cortex, and is therefore an inappropriate tracer to use for mapping D$_2$ densities in the cortex, but we show its comparison to FLB457 and another D$_2$ tracer, fallypride, for completeness [2, 28, 72]; (3) the chosen carfentanil (MOR) map was collated across carfentanil images in the PET Turku Centre database—since our alternative map is a partly overlapping subset of participants, we did not combine the tracers into a single mean map [75, 172].

Synapse density. Synapse density in the cortex was measured in 76 healthy adults (45 males, 48.9 ± 18.4 years of age) by administering $[^{11}C]$UCB-J, a PET tracer that binds to the synaptic vesicle glycoprotein 2A (SV2A) [18, 22, 23, 44–46, 66, 96, 112, 123, 156, 187]. Data were collected on an HRRT PET camera for 90 minutes post injection. Non-displaceable binding potential ($\mathrm{BP_{ND}}$) was modelled using SRTM2, with the centrum semiovale as reference and k_2' fixed to 0.027 (population value). This group-averaged map was first presented in Hansen et al. [62].

Autoradiography receptor data acquisition

Receptor autoradiography data were originally acquired as described in [194]. 15 neurotransmitter receptor densities across 44 cytoarchitectonically defined areas were collected in three post-mortem brains (age range: 72–77, 2 males). See Table S1 for a complete list of receptors included in the autoradiography dataset, Supplementary Table 2 in [194] for the originally reported receptor densities, and https://github.com/AlGoulas/receptor_principles for machine-readable Python *numpy* files of receptor densities [59]. To best compare PET data analyses with the autoradiography dataset, a region-to-region mapping was manually created between the 44 available cortical areas in the autoradiography dataset and the 50 left hemisphere cortical Schaefer-100 regions. Four regions in the Schaefer atlas did not have a suitable mapping to the autoradiography atlas. As such, the 44-region autoradiography atlas was converted to 46 Schaefer left hemisphere regions. Finally, receptor densities were concatenated and z-scored to create a single map of receptor densities across the cortex.

Structural and functional data acquisition

Following the procedure described in de Wael et al. [30], we obtained structural and functional magnetic resonance imaging (MRI) data for 326 unrelated participants (age range 22–35 years, 145 males) from the Human Connectome Project (HCP; S900 release [177]). All four resting state fMRI scans (two scans (R/L and L/R phase encoding directions) on day 1 and two scans (R/L and L/R phase encoding directions) on day 2, each about 15 min long; TR=720 ms), as well as diffusion weighted imaging (DWI) data were available for all participants. All the structural and functional MRI data were pre-processed using HCP minimal pre-processing pipelines [57, 177]. We provide a brief description of data pre-processing below, while detailed information regarding data acquisition and pre-processing is available elsewhere [57, 177].

Structural network reconstruction

DWI data was pre-processed using the MRtrix3 package [171] (https://www.mrtrix.org/). More specifically, fiber orientation distributions were generated using the multi-shell multi-tissue constrained spherical deconvolution algorithm from MRtrix [34, 73]. White matter edges were then reconstructed using probabilistic streamline tractography based on the generated fiber orientation distributions [170]. The tract weights were then optimized by estimating an appropriate cross-section multiplier for each streamline following the procedure proposed by Smith et al. [158] and a connectivity matrix was built for each participant using the 100-region Schaefer parcellation [139]. A group-consensus binary network was constructed using a method that preserves the density and edge-length distributions of the individual connectomes [17, 98, 99]. Edges in the group-consensus network were assigned weights by averaging the log-transformed streamline count of non-zero edges across participants. Edge weights were then scaled to values between 0 and 1.

Functional network reconstruction

All 3T functional MRI time-series were corrected for gradient nonlinearity, head motion using a rigid body transformation, and geometric distortions using scan pairs with opposite phase encoding directions (R/L, L/R) [30]. Further pre-processing steps include co-registration of the corrected images to the T1w structural MR images, brain extraction, normalization of whole brain intensity, high-pass filtering (>2000s FWHM; to correct for scanner drifts), and removing additional noise using the ICA-FIX process [30, 131]. The pre-processed time-series were then parcellated to 100 cortical brain regions according to the Schaefer atlas [139]. The parcellated time-series were used to construct functional connectivity matrices as a Pearson correlation coefficient between pairs of regional time-series for each of the four scans of each participant. A group-average functional connectivity matrix was constructed as the mean functional connectivity across all individuals and scans.

Structure-function coupling

At each brain region, a simple linear regression model was used to predict functional connectivity from communicability. Communicability is defined as the weighted average of all walks and paths between two brain regions, and represents diffusive communication [26, 42]. Additionally, communicability has been previously demonstrated as an important bridge between brain structure and function [41, 60, 144]. In the receptor-informed model, receptor similarity between the region of interest and every other region was included as an additional independent variable. Coupling was defined as the adjusted R^2 of the model. The significance of the receptor-informed structure-function coupling was assessed against a null distribution of adjusted R^2 from a model that adds a rotated regional receptor similarity vector (10 000 repetitions). This ensures that the increase in R^2 when receptor information is included in the model is robust against the addition of a random variable with identical spatial autocorrelation.

MEG power

6-minute resting state eyes-open magenetoencephalography (MEG) time-series were acquired from the Human Connectome Project (HCP, S1200 release) for 33 unrelated participants (age range 22—35, 17 males) [57, 177]. Complete MEG acquisition protocols can be found in the HCP S1200 Release Manual. For each participant, we computed the power spectrum at the vertex level across six different frequency bands: delta (2–4 Hz), theta (5–7 Hz), alpha (8–12 Hz), beta (15–29 Hz), low gamma (30–59 Hz), and high gamma (60–90 Hz), using the open-source software, Brainstorm [166]. The preprocessing was performed by applying notch filters at 60, 120, 180, 240, and 300 Hz, and was followed by a high-pass filter at 0.3 Hz to remove slow-wave and DC-offset artifacts. Preprocessed sensor-level data was used to obtain a source estimation on HCP's fsLR4k cortex surface for each participant. Head models were computed using overlapping spheres and the data and noise covariance matrices were estimated from the resting state MEG and noise recordings. Brainstorm's linearly constrained minimum variance (LCMV) beamformers method was applied to obtain the source activity for each participant. Welch's method was then applied to estimate power spectrum density (PSD) for the source-level data, using overlapping windows of length 4 seconds with 50% overlap. Average power at each frequency band was then calculated for each vertex (i.e. source). Source-level power data was then parcellated into 100 cortical regions for each frequency band [139].

ENIGMA cortical abnormality maps

The ENIGMA (Enhancing Neuroimaging Genetics through Meta-Analysis) Consortium is a data-sharing initiative that relies on standardized image acquisition and processing pipelines, such that disorder maps are comparable [169]. Patterns of cortical abnormality were collected for thirteen neurological, neurodevelopmental, and psychiatric disorders from the ENIGMA consortium and the Enigma toolbox (https://github.com/MICA-MNI/ENIGMA; [84]) including: 22q11.2 deletion syndrome (22q) [165], attention deficit hyperactivity disorder (ADHD) [67], autism spectrum disorder (ASD) [179], idiopathic generalized epilepsy [188], right temporal lobe epilepsy [188], left temporal lobe epilepsy [188], depression [140], obsessive-compulsive disorder (OCD) [19], schizophrenia [176], bipolar disorder (BD) [64], obesity [111], schizotypy [79], and Parkinson's disease (PD) [83]. While most disorders show decreases in cortical thickness, some (e.g. 22q, ASD, schizotypy) also show regional increases in cortical thickness. We therefore refer to the disorder profiles as "cortical abnormalities". Altogether, over 21 000 patients were scanned across the thirteen disorders, against almost 26 000 controls. The values for each map are z-scored effect sizes (Cohen's d) of cortical thickness in patient populations versus healthy controls. Note that the native and only representatin of ENIGMA datasets is the Desikan-Killiany atlas (68 cortical regions) [33]. For visualization purposes, data are inverted such that larger values represent greater cortical thinning. Imaging and processing protocols can be found at http://enigma.ini.usc.edu/protocols/.

Dominance analysis

Dominance analysis seeks to determine the relative contribution ("dominance") of each independent variable to the overall fit (adjusted R^2) of the multiple linear regression model (https://github.com/dominance-analysis/dominance-analysis [7, 20]). This is done by fitting the same regression model on every combination of input variables ($2^p - 1$ submodels for a model with p input variables). Total dominance is defined as the average of the relative increase in R^2 when adding a single input variable of interest to a submodel, across all $2^p - 1$ submodels. The sum of the dominance of all input variables is equal to the total adjusted R^2 of the complete model, making total dominance an intuitive method that partitions the total effect size across predictors. Therefore, unlike other methods of assessing predictor importance, such as methods based on regression coefficients or univariate correlations, dominance analysis accounts for predictor-predictor interactions and is interpretable. Dominance was then normalized by the total fit (R^2_{adj}) of the model, to make dominance fully comparable both within and across models.

Cognitive meta-analytic activation

Probabilistic measures of the association between voxels and cognitive processes were obtained from Neurosynth, a meta-analytic tool that synthesizes results from more than 15 000 published fMRI studies by searching for high-frequency key words (such as "pain" and "attention") that are published alongside fMRI voxel coordinates (https://github.com/neurosynth/neurosynth, using the volumetric association test maps [190]). This measure of association is the probability that a given cognitive process is reported in the study if there is activation observed at a given voxel. Although more than a thousand cognitive processes are reported in Neurosynth, we focus primarily on cognitive function and therefore limit the terms of interest to cognitive and behavioural terms. These terms were selected from the Cognitive Atlas, a public ontology of cognitive science [120], which includes a comprehensive list of neurocognitive processes and has been previously used in conjunction with Neurosynth [3]. We used 123 terms, ranging from umbrella terms (“attention”, “emotion”) to specific cognitive processes (“visual attention”, “episodic memory”), behaviours (“eating”, “sleep”), and emotional states (“fear”, “anxiety”). The coordinates reported by Neurosynth were parcellated according to the Schaefer-100 atlas and z-scored [139]. The probabilistic measure reported by Neurosynth can be interpreted as a quantitative representation of how regional fluctuations in activity are related to psychological processes. The full list of cognitive processes is shown in Table S2.

Partial least squares analysis

Partial least squares analysis (PLS) was used to relate neurotransmitter receptor distributions to functional activation. PLS is an unsupervised multivariate statistical technique that decomposes the two datasets into orthogonal sets of latent variables with maximum covariance [82, 95]. The latent variables consist of receptor weights, cognitive weights, and a singular value which represents the covariance between receptor distributions and functional activations that is explained by the latent variable. Receptor and cognitive scores are computed by projecting the original data onto the respective weights, such that each brain region is assigned a receptor and cognitive score. Finally, receptor loadings are computed as the Pearson’s correlation between receptor densities and receptor scores, and vice versa for cognitive loadings. Note that PLS analysis does not (1) speak to causal relationships between receptors and cognition, (2) make specific univariate receptor-cognition associations, and (3) preclude the existence of additional relationships between receptors and cognitive function.

The significance of the latent variable was assessed on the singular value, against the spin-test (see *Null models*). In the present report, only the first latent variable was significant; remaining latent variables were not analyzed further. Finally, the correlation between receptor and cognitive scores was cross-validated (see *Distance-dependent cross-validation*). The empirical correlation between receptor and cognitive scores across all brain regions was $r(98) = 0.71$, the mean training set correlation was $r(98) = 0.72$, and the mean test set correlation was $r(98) = 0.60$, $p_{\text{spin}} = 0.03$, one-sided.

Distance-dependent cross-validation

The robustness of each multilinear model was assessed by cross-validating the model by using a distance-dependent method [61]. Specifically, this method was applied to every multilinear regression model (Fig. 3c, 4, 6) and the PLS model (Fig. 5). For each brain region (source node), we select the 75% closest regions as the training set, and the remaining 25% of brain regions as the test set, for a total of 100 repetitions in the Schaefer atlas and 68 repetitions in the Desikan-Killiany atlas. This stratification procedure minimizes the dependence among the two sets due to spatial autocorrelation. In the case of multilinear regression models, the model was fit on the training set, and the predicted test-set output variable (regional functional connectivity, MEG power, or disorder maps) was correlated to the empirical test set values. The distribution of Pearson’s correlations between predicted and empirical variables across all repetitions (i.e. all brain regions) can be found in Fig. S4 (structure-function coupling), Fig. S5 (MEG power), and Fig. S8 (disorder maps).

In the case of the PLS analysis, the model was fit on the training set and the weights were projected onto the test set to calculate predicted receptor and cognitive scores. Training and test sets were defined as described above, and the procedure was repeated for each brain region as the source node (100 repetitions). The correlation between receptor and cognitive score was separately calculated in the training and test set. The significance of the mean out-of-sample correlation was assessed against a permuted null model, constructed by repeating the cross-validation on spatial autocorrelation-preserving permutations of the functional association matrix (1 000 repetitions, Fig. 5d).

Null models

Spatial autocorrelation-preserving permutation tests were used to assess statistical significance of associations across brain regions, termed “spin tests” [3, 91, 180]. We created a surface-based representation of the parcellation on the FreeSurfer fsaverage surface, via files from the Connectome Mapper toolkit (https://github.com/LTS5/cmp). We used the spherical projection of the fsaverage surface to define spatial coordinates for each parcel by selecting the coordinates of the vertex closest to the center of the mass of each parcel [181]. These parcel coordinates were then randomly rotated, and original parcels were reassigned the value of the closest rotated parcel (10 000 repetitions). Parcels for which the medial wall was closest were assigned the value of the next most proximal parcel instead. The procedure was performed at the parcel resolution rather than the vertex resolution to avoid upsampling the data, and to each hemisphere separately. Note that the spin test was not applied to autroadiography data because of missing samples. A permutation test was applied instead.

A second null model was used to test whether receptor similarity is greater in connected regions than unconnected regions. This model generates a null structural connectome that preserves the density, edge length, and degree distributions of the empirical structural connectome [16, 58, 128, 180]. Briefly, edges were binned according to Euclidean distance. Within each bin, pairs of edges were selected at random and swapped. This procedure was then repeated 10 000 times. To compute a p-value, the mean receptor similarity of unconnected edges was subtracted from the mean receptor similarity of connected edges, and this difference was compared to a null distribution of differences computed on the rewired networks.

Acknowledgments

We thank Vincent Bazinet, Zhen-Qi Liu, Filip Milisav, Laura Suarez, Bertha Vazquez-Rodriguez, and Mingze Li for their comments and suggestions on the manuscript. This research was undertaken thanks in part to funding from the Canada First Research Excellence Fund, awarded to McGill University for the Healthy Brains for Healthy Lives initiative. BM acknowledges support from the Natural Sciences and Engineering Research Council of Canada (NSERC Discovery Grant RGPIN #017-04265) and from the Canada Research Chairs Program. JYH acknowledges support from the Helmholtz International BigBrain Analytics & Learning Laboratory, the Natural Sciences and Engineering Research Council of Canada, and the Fonds de reserches de Québec. The funders had no role in study design, data collection and analysis, decision to publish or preparation of the manuscript.

[1] Aghourian, M., Legault-Denis, C., Soucy, J., Rosa-Neto, P., Gauthier, S., Kostikov, A., Gravel, P., and Bedard, M. (2017). Quantification of brain cholinergic denervation in alzheimer's disease using pet imaging with [18 f]-feobv. *Molecular psychiatry*, 22(11):1531–1538.

[2] Alakurtti, K., Johansson, J. J., Joutsa, J., Laine, M., Bäckman, L., Nyberg, L., and Rinne, J. O. (2015). Long-term test–retest reliability of striatal and extrastriatal dopamine d2/3 receptor binding: study with [11c] raclopride and high-resolution pet. *Journal of Cerebral Blood Flow & Metabolism*, 35(7):1199–1205.

[3] Alexander-Bloch, A. F., Shou, H., Liu, S., Satterthwaite, T. D., Glahn, D. C., Shinohara, R. T., Vandekar, S. N., and Raznahan, A. (2018). On testing for spatial correspondence between maps of human brain structure and function. *NeuroImage*, 178:540–551.

[4] Anderson, K. M., Collins, M. A., Chin, R., Ge, T., Rosenberg, M. D., and Holmes, A. J. (2020). Transcriptional and imaging-genetic association of cortical interneurons, brain function, and schizophrenia risk. *Nature communications*, 11(1):1–15.

[5] Arnatkeviciute, A., Fulcher, B., Bellgrove, M., and Fornito, A. (2021). Where the genome meets the connectome: understanding how genes shape human brain connectivity. *Neuroimage*.

[6] Avena-Koenigsberger, A., Misic, B., and Sporns, O. (2018). Communication dynamics in complex brain networks. *Nature Reviews Neuroscience*, 19(1):17–33.

[7] Azen, R. and Budescu, D. V. (2003). The dominance analysis approach for comparing predictors in multiple regression. *Psychological methods*, 8(2):129.

[8] Baillet, S. (2017). Magnetoencephalography for brain electrophysiology and imaging. *Nature neuroscience*, 20(3):327–339.

[9] Baldassarri, S. R., Hillmer, A. T., Anderson, J. M., Jatlow, P., Nabulsi, N., Labaree, D., Cosgrove, K. P., O'Malley, S. S., Eissenberg, T., Krishnan-Sarin, S., et al. (2018). Use of electronic cigarettes leads to significant beta2-nicotinic acetylcholine receptor occupancy: evidence from a pet imaging study. *Nicotine and Tobacco Research*, 20(4):425–433.

[10] Baldassarri, S. R., Park, E., Finnema, S. J., Planeta, B., Nabulsi, N., Najafzadeh, S., Ropchan, J., Huang, Y., Hannestad, J., Maloney, K., et al. (2020). Inverse changes in raphe and cortical 5-ht1b receptor availability after acute tryptophan depletion in healthy human subjects. *Synapse*, 74(10):e22159.

[11] Bedard, M.-A., Aghourian, M., Legault-Denis, C., Postuma, R. B., Soucy, J.-P., Gagnon, J.-F., Pelletier, A., and Montplaisir, J. (2019). Brain cholinergic alterations in idiopathic rem sleep behaviour disorder: a pet imaging study with 18f-feobv. *Sleep medicine*, 58:35–41.

[12] Belfort-DeAguiar, R., Gallezot, J.-D., Hwang, J. J., Elshafie, A., Yeckel, C. W., Chan, O., Carson, R. E., Ding, Y.-S., and Sherwin, R. S. (2018). Noradrenergic activity in the human brain: a mechanism supporting the defense against hypoglycemia. *The Journal of Clinical Endocrinology & Metabolism*, 103(6):2244–2252.

[13] Beliveau, V., Ganz, M., Feng, L., Ozenne, B., Højgaard, L., Fisher, P. M., Svarer, C., Greve, D. N., and Knudsen, G. M. (2017). A high-resolution in vivo atlas of the human brain's serotonin system. *Journal of Neuroscience*, 37(1):120–128.

[14] Bellec, P., Perlbarg, V., Jbabdi, S., Pélégrini-Issac, M., Anton, J.-L., Doyon, J., and Benali, H. (2006). Identification of large-scale networks in the brain using fmri. *Neuroimage*, 29(4):1231–1243.

[15] Benjamini, Y. and Hochberg, Y. (1995). Controlling the false discovery rate: a practical and powerful approach to multiple testing. *J Roy Stat Soc B*, 57(1):289–300.

[16] Betzel, R. F. and Bassett, D. S. (2018). Specificity and robustness of long-distance connections in weighted, inter-

areal connectomes. *Proceedings of the National Academy of Sciences*, 115(21):E4880–E4889.

[17] Betzel, R. F., Griffa, A., Hagmann, P., and Mišić, B. (2019). Distance-dependent consensus thresholds for generating group-representative structural brain networks. *Network neuroscience*, 3(2):475–496.

[18] Bini, J., Holden, D., Fontaine, K., Mulnix, T., Lu, Y., Matuskey, D., Ropchan, J., Nabulsi, N., Huang, Y., and Carson, R. E. (2020). Human adult and adolescent biodistribution and dosimetry of the synaptic vesicle glycoprotein 2a radioligand 11 c-ucb-j. *EJNMMI research*, 10(1):1–8.

[19] Boedhoe, P. S., Schmaal, L., Abe, Y., Alonso, P., Ameis, S. H., Anticevic, A., Arnold, P. D., Batistuzzo, M. C., Benedetti, F., Beucke, J. C., et al. (2018). Cortical abnormalities associated with pediatric and adult obsessive-compulsive disorder: findings from the enigma obsessive-compulsive disorder working group. *American Journal of Psychiatry*, 175(5):453–462.

[20] Budescu, D. V. (1993). Dominance analysis: a new approach to the problem of relative importance of predictors in multiple regression. *Psychological bulletin*, 114(3):542.

[21] Burt, J. B., Demirtaş, M., Eckner, W. J., Navejar, N. M., Ji, J. L., Martin, W. J., Bernacchia, A., Anticevic, A., and Murray, J. D. (2018). Hierarchy of transcriptomic specialization across human cortex captured by structural neuroimaging topography. *Nature neuroscience*, 21(9):1251–1259.

[22] Chen, M.-K., Mecca, A. P., Naganawa, M., Finnema, S. J., Toyonaga, T., Lin, S.-f., Najafzadeh, S., Ropchan, J., Lu, Y., McDonald, J. W., et al. (2018). Assessing synaptic density in alzheimer disease with synaptic vesicle glycoprotein 2a positron emission tomographic imaging. *JAMA neurology*, 75(10):1215–1224.

[23] Chen, M.-K., Mecca, A. P., Naganawa, M., Gallezot, J.-D., Toyonaga, T., Mondal, J., Finnema, S. J., Lin, S.-f., O'Dell, R. S., McDonald, J. W., et al. (2021). Comparison of [11c] ucb-j and [18f] fdg pet in alzheimer's disease: A tracer kinetic modeling study. *Journal of Cerebral Blood Flow & Metabolism*, page 0271678X211004312.

[24] Chiang-shan, R. L., Potenza, M. N., Lee, D. E., Planeta, B., Gallezot, J.-D., Labaree, D., Henry, S., Nabulsi, N., Sinha, R., Ding, Y.-S., et al. (2014). Decreased norepinephrine transporter availability in obesity: positron emission tomography imaging with (s, s)-[11c] o-methylreboxetine. *Neuroimage*, 86:306–310.

[25] Costa, C., Parnetti, L., D'Amelio, M., Tozzi, A., Tantucci, M., Romigi, A., Siliquini, S., Cavallucci, V., Di Filippo, M., Mazzocchetti, P., et al. (2016). Epilepsy, amyloid-β, and d1 dopamine receptors: a possible pathogenetic link? *Neurobiology of aging*, 48:161–171.

[26] Crofts, J. J. and Higham, D. J. (2009). A weighted communicability measure applied to complex brain networks. *Journal of the Royal Society Interface*, 6(33):411–414.

[27] Cuypers, K., Hehl, M., van Aalst, J., Chalavi, S., Mikkelsen, M., Van Laere, K., Dupont, P., Mantini, D., and Swinnen, S. P. (2021). Age-related gabaergic differences in the primary sensorimotor cortex: A multimodal approach combining pet, mrs and tms. *Neuroimage*, 226:117536.

[28] Dagher, A. and Palomero-Gallagher, N. (2020). Mapping dopamine with positron emission tomography: A note of caution. *Neuroimage*.

[29] DasBanerjee, T., Middleton, F. A., Berger, D. F., Lombardo, J. P., Sagvolden, T., and Faraone, S. V. (2008). A comparison of molecular alterations in environmental and genetic rat models of adhd: a pilot study. *American Journal of Medical Genetics Part B: Neuropsychiatric Genetics*, 147(8):1554–1563.

[30] de Wael, R. V., Larivière, S., Caldairou, B., Hong, S.-J., Margulies, D. S., Jefferies, E., Bernasconi, A., Smallwood, J., Bernasconi, N., and Bernhardt, B. C. (2018). Anatomical and microstructural determinants of hippocampal subfield functional connectome embedding. *Proceedings of the National Academy of Sciences*, 115(40):10154–10159.

[31] Deco, G., Vidaurre, D., and Kringelbach, M. L. (2021). Revisiting the global workspace orchestrating the hierarchical organization of the human brain. *Nature human behaviour*, 5(4):497–511.

[32] Demirtaş, M., Burt, J. B., Helmer, M., Ji, J. L., Adkinson, B. D., Glasser, M. F., Van Essen, D. C., Sotiropoulos, S. N., Anticevic, A., and Murray, J. D. (2019). Hierarchical heterogeneity across human cortex shapes large-scale neural dynamics. *Neuron*, 101(6):1181–1194.

[33] Desikan, R. S., Ségonne, F., Fischl, B., Quinn, B. T., Dickerson, B. C., Blacker, D., Buckner, R. L., Dale, A. M., Maguire, R. P., Hyman, B. T., et al. (2006). An automated labeling system for subdividing the human cerebral cortex on mri scans into gyral based regions of interest. *NeuroImage*, 31(3):968–980.

[34] Dhollander, T., Raffelt, D., and Connelly, A. (2016). Unsupervised 3-tissue response function estimation from single-shell or multi-shell diffusion mr data without a co-registered t1 image. In *ISMRM Workshop on Breaking the Barriers of Diffusion MRI*, volume 5. ISMRM.

[35] Ding, Y.-S., Singhal, T., Planeta-Wilson, B., Gallezot, J.-D., Nabulsi, N., Labaree, D., Ropchan, J., Henry, S., Williams, W., Carson, R. E., et al. (2010). Pet imaging of the effects of age and cocaine on the norepinephrine transporter in the human brain using (s, s)-[11c] o-methylreboxetine and hrrt. *Synapse*, 64(1):30–38.

[36] DuBois, J. M., Rousset, O. G., Rowley, J., Porras-Betancourt, M., Reader, A. J., Labbe, A., Massarweh, G., Soucy, J.-P., Rosa-Neto, P., and Kobayashi, E. (2016). Characterization of age/sex and the regional distribution of mglur5 availability in the healthy human brain measured by high-resolution [11 c] abp688 pet. *European journal of nuclear medicine and molecular imaging*, 43(1):152–162.

[37] Dukart, J., Holiga, Š., Chatham, C., Hawkins, P., Forsyth, A., McMillan, R., Myers, J., Lingford-Hughes, A. R., Nutt, D. J., Merlo-Pich, E., et al. (2018). Cerebral blood flow predicts differential neurotransmitter activity. *Scientific reports*, 8(1):1–11.

[38] Dukart, J., Holiga, S., Rullmann, M., Lanzenberger, R., Hawkins, P. C., Mehta, M. A., Hesse, S., Barthel, H., Sabri, O., Jech, R., et al. (2021). Juspace: A tool for spatial correlation analyses of magnetic resonance imaging data with nuclear imaging derived neurotransmitter maps. Technical report, Wiley Online Library.

[39] D'Souza, D. C., Cortes-Briones, J. A., Ranganathan, M., Thurnauer, H., Creatura, G., Surti, T., Planeta, B., Neumeister, A., Pittman, B., Normandin, M. D., et al. (2016). Rapid changes in cannabinoid 1 receptor availability in cannabis-dependent male subjects after absti-

nence from cannabis. *Biological psychiatry: cognitive neuroscience and neuroimaging*, 1(1):60–67.

[40] Erritzoe, D., Holst, K., Frokjaer, V. G., Licht, C. L., Kalbitzer, J., Nielsen, F. Å., Svarer, C., Madsen, J., and Knudsen, G. M. (2010). A nonlinear relationship between cerebral serotonin transporter and 5-ht2a receptor binding: an in vivo molecular imaging study in humans. *Journal of Neuroscience*, 30(9):3391–3397.

[41] Esfahlani, F. Z., Faskowitz, J., Slack, J., Mišić, B., and Betzel, R. F. (2021). Local structure-function relationships in human brain networks across the human lifespan. *bioRxiv*.

[42] Estrada, E. and Hatano, N. (2008). Communicability in complex networks. *Physical Review E*, 77(3):036111.

[43] Evans, A. C. (2013). Networks of anatomical covariance. *Neuroimage*, 80:489–504.

[44] Finnema, S. J., Nabulsi, N. B., Mercier, J., Lin, S.-f., Chen, M.-K., Matuskey, D., Gallezot, J.-D., Henry, S., Hannestad, J., Huang, Y., et al. (2018). Kinetic evaluation and test–retest reproducibility of [11c] ucb-j, a novel radioligand for positron emission tomography imaging of synaptic vesicle glycoprotein 2a in humans. *Journal of Cerebral Blood Flow & Metabolism*, 38(11):2041–2052.

[45] Finnema, S. J., Rossano, S., Naganawa, M., Henry, S., Gao, H., Pracitto, R., Maguire, R. P., Mercier, J., Kervyn, S., Nicolas, J.-M., et al. (2019). A single-center, open-label positron emission tomography study to evaluate brivaracetam and levetiracetam synaptic vesicle glycoprotein 2a binding in healthy volunteers. *Epilepsia*, 60(5):958–967.

[46] Finnema, S. J., Toyonaga, T., Detyniecki, K., Chen, M.-K., Dias, M., Wang, Q., Lin, S.-F., Naganawa, M., Gallezot, J.-D., Lu, Y., et al. (2020). Reduced synaptic vesicle protein 2a binding in temporal lobe epilepsy: A [11c] ucb-j positron emission tomography study. *Epilepsia*, 61(10):2183–2193.

[47] Forstmann, B. U., de Hollander, G., van Maanen, L., Alkemade, A., and Keuken, M. C. (2017). Towards a mechanistic understanding of the human subcortex. *Nature Reviews Neuroscience*, 18(1):57–65.

[48] Froudist-Walsh, S., Xu, T., Niu, M., Rapan, L., Zilles, K., Margulies, D. S., Wang, X.-J., and Palomero-Gallagher, N. (2021). Gradients of receptor expression in the macaque cortex. *bioRxiv*.

[49] Fulcher, B. D. and Fornito, A. (2016). A transcriptional signature of hub connectivity in the mouse connectome. *Proc Natl Acad Sci USA*, 113(5):1435–1440.

[50] Funck, T., Wagstyl, K., Omidyeganeh, M., Lepage, C., Toussaint, P., Zilles, K., Thiel, A., Evans, A., and Palomero-Gallagher, N. (2021). 3d reconstruction of 20 neurotransmitter receptor atlases from 2d autoradiographs. *27th Annual Meeting of the Organization for Human Brain Mapping*.

[51] Gallezot, J.-D., Nabulsi, N., Neumeister, A., Planeta-Wilson, B., Williams, W. A., Singhal, T., Kim, S., Maguire, R. P., McCarthy, T., Frost, J. J., et al. (2010). Kinetic modeling of the serotonin 5-ht1b receptor radioligand [11c] p943 in humans. *Journal of Cerebral Blood Flow & Metabolism*, 30(1):196–210.

[52] Gallezot, J.-D., Planeta, B., Nabulsi, N., Palumbo, D., Li, X., Liu, J., Rowinski, C., Chidsey, K., Labaree, D., Ropchan, J., et al. (2017). Determination of receptor occupancy in the presence of mass dose:[11c] gsk189254 pet imaging of histamine h3 receptor occupancy by pf-03654746. *Journal of Cerebral Blood Flow & Metabolism*, 37(3):1095–1107.

[53] Galovic, M., Al-Diwani, A., Vivekananda, U., Torrealdea, F., Erlandsson, K., Fryer, T. D., Hong, Y. T., Thomas, B. A., McGinnity, C. J., Edmond, E., et al. (2021a). In vivo nmda receptor function in people with nmda receptor antibody encephalitis. *medRxiv*.

[54] Galovic, M., Erlandsson, K., Fryer, T. D., Hong, Y. T., Manavaki, R., Sari, H., Chetcuti, S., Thomas, B. A., Fisher, M., Sephton, S., et al. (2021b). Validation of a combined image derived input function and venous sampling approach for the quantification of [18f] ge-179 pet binding in the brain. *NeuroImage*, page 118194.

[55] Gao, R., van den Brink, R. L., Pfeffer, T., and Voytek, B. (2020). Neuronal timescales are functionally dynamic and shaped by cortical microarchitecture. *Elife*, 9:e61277.

[56] Giorgi, F. S., Pizzanelli, C., Biagioni, F., Murri, L., and Fornai, F. (2004). The role of norepinephrine in epilepsy: from the bench to the bedside. *Neuroscience & Biobehavioral Reviews*, 28(5):507–524.

[57] Glasser, M. F., Sotiropoulos, S. N., Wilson, J. A., Coalson, T. S., Fischl, B., Andersson, J. L., Xu, J., Jbabdi, S., Webster, M., Polimeni, J. R., et al. (2013). The minimal preprocessing pipelines for the human connectome project. *Neuroimage*, 80:105–124.

[58] Gollo, L. L., Roberts, J. A., Cropley, V. L., Di Biase, M. A., Pantelis, C., Zalesky, A., and Breakspear, M. (2018). Fragility and volatility of structural hubs in the human connectome. *Nature neuroscience*, 21(8):1107–1116.

[59] Goulas, A., Changeux, J.-P., Wagstyl, K., Amunts, K., Palomero-Gallagher, N., and Hilgetag, C. C. (2021). The natural axis of transmitter receptor distribution in the human cerebral cortex. *Proceedings of the National Academy of Sciences*, 118(3).

[60] Grayson, D. S., Bliss-Moreau, E., Machado, C. J., Bennett, J., Shen, K., Grant, K. A., Fair, D. A., and Amaral, D. G. (2016). The rhesus monkey connectome predicts disrupted functional networks resulting from pharmacogenetic inactivation of the amygdala. *Neuron*, 91(2):453–466.

[61] Hansen, J. Y., Markello, R. D., Vogel, J. W., Seidlitz, J., Bzdok, D., and Misic, B. (2021). Mapping gene transcription and neurocognition across human neocortex. *Nature Human Behaviour*, pages 1–11.

[62] Hansen, J. Y., Shafiei, G. Y., Vogel, J. W., Smart, K., Bearden, C. E., Hoogman, M., Franke, B., van Rooij, D., Buitelaar, J., McDonald, C. R., et al. (2022). Molecular and connectomic vulnerability shape cross-disorder cortical abnormalities. *bioRxiv*.

[63] Hesse, S., Becker, G.-A., Rullmann, M., Bresch, A., Luthardt, J., Hankir, M. K., Zientek, F., Reißig, G., Patt, M., Arelin, K., et al. (2017). Central noradrenaline transporter availability in highly obese, non-depressed individuals. *European journal of nuclear medicine and molecular imaging*, 44(6):1056–1064.

[64] Hibar, D., Westlye, L. T., Doan, N. T., Jahanshad, N., Cheung, J., Ching, C. R., Versace, A., Bilderbeck, A., Uhlmann, A., Mwangi, B., et al. (2018). Cortical abnormalities in bipolar disorder: an mri analysis of 6503 individuals from the enigma bipolar disorder working group. *Molecular psychiatry*, 23(4):932–942.

[65] Hillmer, A. T., Esterlis, I., Gallezot, J.-D., Bois, F., Zheng, M.-Q., Nabulsi, N., Lin, S.-F., Papke, R., Huang, Y., Sabri, O., et al. (2016). Imaging of cerebral $\alpha 4\beta 2$* nicotinic acetylcholine receptors with (-)-[18f] flubatine pet: Implementation of bolus plus constant infusion and sensitivity to acetylcholine in human brain. *Neuroimage*, 141:71–80.

[66] Holmes, S. E., Scheinost, D., Finnema, S. J., Naganawa, M., Davis, M. T., DellaGioia, N., Nabulsi, N., Matuskey, D., Angarita, G. A., Pietrzak, R. H., et al. (2019). Lower synaptic density is associated with depression severity and network alterations. *Nature communications*, 10(1):1–10.

[67] Hoogman, M., Muetzel, R., Guimaraes, J. P., Shumskaya, E., Mennes, M., Zwiers, M. P., Jahanshad, N., Sudre, G., Wolfers, T., Earl, E. A., et al. (2019). Brain imaging of the cortex in adhd: a coordinated analysis of large-scale clinical and population-based samples. *American Journal of Psychiatry*, 176(7):531–542.

[68] Horvát, S., Gămănuț, R., Ercsey-Ravasz, M., Magrou, L., Gămănuț, B., Van Essen, D. C., Burkhalter, A., Knoblauch, K., Toroczkai, Z., and Kennedy, H. (2016). Spatial embedding and wiring cost constrain the functional layout of the cortical network of rodents and primates. *PLoS biology*, 14(7):e1002512.

[69] Huntenburg, J. M., Bazin, P.-L., Goulas, A., Tardif, C. L., Villringer, A., and Margulies, D. S. (2017). A systematic relationship between functional connectivity and intracortical myelin in the human cerebral cortex. *Cerebral Cortex*, 27(2):981–997.

[70] Inoue, M., Suhara, T., Sudo, Y., Okubo, Y., Yasuno, F., Kishimoto, T., Yoshikawa, K., and Tanada, S. (2001). Age-related reduction of extrastriatal dopamine d2 receptor measured by pet. *Life sciences*, 69(9):1079–1084.

[71] Insel, T., Cuthbert, B., Garvey, M., Heinssen, R., Pine, D. S., Quinn, K., Sanislow, C., and Wang, P. (2010). Research domain criteria (rdoc): toward a new classification framework for research on mental disorders. *American Psychiatric Association*.

[72] Jaworska, N., Cox, S. M., Tippler, M., Castellanos-Ryan, N., Benkelfat, C., Parent, S., Dagher, A., Vitaro, F., Boivin, M., Pihl, R. O., et al. (2020). Extra-striatal d 2/3 receptor availability in youth at risk for addiction. *Neuropsychopharmacology*, 45(9):1498–1505.

[73] Jeurissen, B., Tournier, J.-D., Dhollander, T., Connelly, A., and Sijbers, J. (2014). Multi-tissue constrained spherical deconvolution for improved analysis of multi-shell diffusion mri data. *NeuroImage*, 103:411–426.

[74] Kaller, S., Rullmann, M., Patt, M., Becker, G.-A., Luthardt, J., Girbardt, J., Meyer, P. M., Werner, P., Barthel, H., Bresch, A., et al. (2017). Test–retest measurements of dopamine d 1-type receptors using simultaneous pet/mri imaging. *European journal of nuclear medicine and molecular imaging*, 44(6):1025–1032.

[75] Kantonen, T., Karjalainen, T., Isojärvi, J., Nuutila, P., Tuisku, J., Rinne, J., Hietala, J., Kaasinen, V., Kalliokoski, K., Scheinin, H., et al. (2020). Interindividual variability and lateralization of μ-opioid receptors in the human brain. *NeuroImage*, 217:116922.

[76] Karrer, T. M., McLaughlin, C. L., Guaglianone, C. P., and Samanez-Larkin, G. R. (2019). Reduced serotonin receptors and transporters in normal aging adults: a meta-analysis of pet and spect imaging studies. *Neurobiology of aging*, 80:1–10.

[77] Kato, T. (2019). Current understanding of bipolar disorder: toward integration of biological basis and treatment strategies. *Psychiatry and clinical neurosciences*, 73(9):526–540.

[78] Khan, A. F., Adewale, Q., Baumeister, T. R., Carbonell, F., Zilles, K., Palomero-Gallagher, N., Iturria-Medina, Y., and the Alzheimer's Disease Neuroimaging Initiative (2021). Personalized brain models identify neurotransmitter receptor changes in alzheimer's disease. *Brain*.

[79] Kirschner, M., Hodzic-Santor, B., Kircher, T., Krug, A., Meller, T., Grotegerd, D., Fornito, A., Arnatkeviciute, A., Bellgrove, M., Tiego, J., et al. (2021). Cortical and subcortical neuroanatomical signatures of schizotypy in 3,004 individuals assessed in a worldwide enigma study. *medRxiv*.

[80] Knudsen, G. M., Ganz, M., Appelhoff, S., Boellaard, R., Bormans, G., Carson, R. E., Catana, C., Doudet, D., Gee, A. D., Greve, D. N., et al. (2020). Guidelines for the content and format of pet brain data in publications and archives: A consensus paper. *Journal of Cerebral Blood Flow & Metabolism*, 40(8):1576–1585.

[81] Kringelbach, M. L., Cruzat, J., Cabral, J., Knudsen, G. M., Carhart-Harris, R., Whybrow, P. C., Logothetis, N. K., and Deco, G. (2020). Dynamic coupling of whole-brain neuronal and neurotransmitter systems. *Proceedings of the National Academy of Sciences*, 117(17):9566–9576.

[82] Krishnan, A., Williams, L. J., McIntosh, A. R., and Abdi, H. (2011). Partial least squares (pls) methods for neuroimaging: a tutorial and review. *NeuroImage*, 56(2):455–475.

[83] Laansma, M. A., Bright, J. K., Al-Bachari, S., Anderson, T. J., Ard, T., Assogna, F., Baquero, K. A., Berendse, H. W., Blair, J., Cendes, F., et al. (2021). International multicenter analysis of brain structure across clinical stages of parkinson's disease. *Movement Disorders*.

[84] Lariviere, S., Paquola, C., Park, B.-y., Royer, J., Wang, Y., Benkarim, O., de Wael, R. V., Valk, S. L., Thomopoulos, S. I., Kirschner, M., et al. (2020). The enigma toolbox: Cross-disorder integration and multiscale neural contextualization of multisite neuroimaging datasets. *bioRxiv*.

[85] Larivière, S., Paquola, C., Park, B.-y., Royer, J., Wang, Y., Benkarim, O., Vos de Wael, R., Valk, S. L., Thomopoulos, S. I., Kirschner, M., et al. (2021). The enigma toolbox: multiscale neural contextualization of multisite neuroimaging datasets. *Nature Methods*, 18(7):698–700.

[86] Laurikainen, H., Tuominen, L., Tikka, M., Merisaari, H., Armio, R.-L., Sormunen, E., Borgan, F., Veronese, M., Howes, O., Haaparanta-Solin, M., et al. (2019). Sex difference in brain cb1 receptor availability in man. *Neuroimage*, 184:834–842.

[87] Leko, M. B., Hof, P. R., and Šimić, G. (2021). Alterations and interactions of subcortical modulatory systems in alzheimer's disease. *Progress in brain research*, 261:379–421.

[88] Lerma, J. and Marques, J. M. (2013). Kainate receptors in health and disease. *Neuron*, 80(2):292–311.

[89] Mahjoory, K., Schoffelen, J.-M., Keitel, A., and Gross, J. (2020). The frequency gradient of human resting-state brain oscillations follows cortical hierarchies. *Elife*, 9:e53715.

[90] Markello, R. D., Hansen, J. Y., Liu, Z.-Q., Bazinet, V., Shafiei, G., Suarez, L. E., Blostein, N., Seidlitz, J., Bail-

let, S., Satterthwaite, T. D., et al. (2022). Neuromaps: structural and functional interpretation of brain maps. *bioRxiv*.

[91] Markello, R. D. and Misic, B. (2021). Comparing spatial null models for brain maps. *NeuroImage*, page 118052.

[92] Martins, D., Giacomel, A., Williams, S. C., Turkheimer, F. E., Dipasquale, O., Veronese, M., templates working group, P., et al. (2021). Imaging transcriptomics: Convergent cellular, transcriptomic, and molecular neuroimaging signatures in the healthy adult human brain. *bioRxiv*.

[93] Matuskey, D., Bhagwagar, Z., Planeta, B., Pittman, B., Gallezot, J.-D., Chen, J., Wanyiri, J., Najafzadeh, S., Ropchan, J., Geha, P., et al. (2014). Reductions in brain 5-ht1b receptor availability in primarily cocaine-dependent humans. *Biological psychiatry*, 76(10):816–822.

[94] McGinnity, C. J., Hammers, A., Barros, D. A. R., Luthra, S. K., Jones, P. A., Trigg, W., Micallef, C., Symms, M. R., Brooks, D. J., Koepp, M. J., et al. (2014). Initial evaluation of 18f-ge-179, a putative pet tracer for activated n-methyl d-aspartate receptors. *Journal of Nuclear Medicine*, 55(3):423–430.

[95] McIntosh, A. R. and Mišić, B. (2013). Multivariate statistical analyses for neuroimaging data. *Annu Rev Psychol*, 64:499–525.

[96] Mecca, A. P., Chen, M.-K., O'Dell, R. S., Naganawa, M., Toyonaga, T., Godek, T. A., Harris, J. E., Bartlett, H. H., Zhao, W., Nabulsi, N. B., et al. (2020). In vivo measurement of widespread synaptic loss in alzheimer's disease with sv2a pet. *Alzheimer's & Dementia*, 16(7):974–982.

[97] Mesulam, M.-M. (1998). From sensation to cognition. *Brain*, 121(6):1013–1052.

[98] Mišić, B., Betzel, R. F., Griffa, A., De Reus, M. A., He, Y., Zuo, X.-N., Van Den Heuvel, M. P., Hagmann, P., Sporns, O., and Zatorre, R. J. (2018). Network-based asymmetry of the human auditory system. *Cerebral Cortex*, 28(7):2655–2664.

[99] Mišić, B., Betzel, R. F., Nematzadeh, A., Goni, J., Griffa, A., Hagmann, P., Flammini, A., Ahn, Y.-Y., and Sporns, O. (2015). Cooperative and competitive spreading dynamics on the human connectome. *Neuron*, 86(6):1518–1529.

[100] Murray, J. D., Bernacchia, A., Freedman, D. J., Romo, R., Wallis, J. D., Cai, X., Padoa-Schioppa, C., Pasternak, T., Seo, H., Lee, D., et al. (2014). A hierarchy of intrinsic timescales across primate cortex. *Nature neuroscience*, 17(12):1661–1663.

[101] Murrough, J. W., Czermak, C., Henry, S., Nabulsi, N., Gallezot, J.-D., Gueorguieva, R., Planeta-Wilson, B., Krystal, J. H., Neumaier, J. F., Huang, Y., et al. (2011a). The effect of early trauma exposure on serotonin type 1b receptor expression revealed by reduced selective radioligand binding. *Archives of general psychiatry*, 68(9):892–900.

[102] Murrough, J. W., Henry, S., Hu, J., Gallezot, J.-D., Planeta-Wilson, B., Neumaier, J. F., and Neumeister, A. (2011b). Reduced ventral striatal/ventral pallidal serotonin 1b receptor binding potential in major depressive disorder. *Psychopharmacology*, 213(2):547–553.

[103] Naganawa, M., Nabulsi, N., Henry, S., Matuskey, D., Lin, S.-F., Slieker, L., Schwarz, A. J., Kant, N., Jesudason, C., Ruley, K., et al. (2021). First-in-human assessment of 11c-lsn3172176, an m1 muscarinic acetylcholine receptor pet radiotracer. *Journal of Nuclear Medicine*, 62(4):553–560.

[104] Neumeister, A., Normandin, M. D., Murrough, J. W., Henry, S., Bailey, C. R., Luckenbaugh, D. A., Tuit, K., Zheng, M.-Q., Galatzer-Levy, I. R., Sinha, R., et al. (2012). Positron emission tomography shows elevated cannabinoid cb 1 receptor binding in men with alcohol dependence. *Alcoholism: Clinical and Experimental Research*, 36(12):2104–2109.

[105] Nordin, K., Gorbach, T., Pedersen, R., Panes Lundmark, V., Johansson, J., Andersson, M., McNulty, C., Riklund, K., Wåhlin, A., Papenberg, G., et al. (2022). Dynamic: A prospective longitudinal study of dopamine and brain connectomes: A new window into cognitive aging. *Journal of Neuroscience Research*.

[106] Nørgaard, M., Beliveau, V., Ganz, M., Svarer, C., Pinborg, L. H., Keller, S. H., Jensen, P. S., Greve, D. N., and Knudsen, G. M. (2021). A high-resolution in vivo atlas of the human brain's benzodiazepine binding site of gabaa receptors. *NeuroImage*, 232:117878.

[107] Nørgaard, M., Ganz, M., Svarer, C., Frokjaer, V. G., Greve, D. N., Strother, S. C., and Knudsen, G. M. (2019). Optimization of preprocessing strategies in positron emission tomography (pet) neuroimaging: A [11c] dasb pet study. *Neuroimage*, 199:466–479.

[108] Norgaard, M., Matheson, G. J., Hansen, H. D., Thomas, A. G., Searle, G., Rizzo, G., Veronese, M., Giacomel, A., Yaqub, M., Tonietto, M., et al. (2021). Pet-bids, an extension to the brain imaging data structure for positron emission tomography. *bioRxiv*.

[109] Normandin, M. D., Zheng, M.-Q., Lin, K.-S., Mason, N. S., Lin, S.-F., Ropchan, J., Labaree, D., Henry, S., Williams, W. A., Carson, R. E., et al. (2015). Imaging the cannabinoid cb1 receptor in humans with [11c] omar: assessment of kinetic analysis methods, test–retest reproducibility, and gender differences. *Journal of Cerebral Blood Flow & Metabolism*, 35(8):1313–1322.

[110] Noudoost, B. and Moore, T. (2011). The role of neuromodulators in selective attention. *Trends in cognitive sciences*, 15(12):585–591.

[111] Opel, N., Thalamuthu, A., Milaneschi, Y., Grotegerd, D., Flint, C., Leenings, R., Goltermann, J., Richter, M., Hahn, T., Woditsch, G., et al. (2020). Brain structural abnormalities in obesity: relation to age, genetic risk, and common psychiatric disorders. *Molecular psychiatry*, pages 1–14.

[112] O'Dell, R. S., Mecca, A. P., Chen, M.-K., Naganawa, M., Toyonaga, T., Lu, Y., Godek, T. A., Harris, J. E., Bartlett, H. H., Banks, E. R., et al. (2021). Association of aβ deposition and regional synaptic density in early alzheimer's disease: a pet imaging study with [11 c] ucb-j. *Alzheimer's Research & Therapy*, 13(1):1–12.

[113] Palomero-Gallagher, N., Vogt, B. A., Schleicher, A., Mayberg, H. S., and Zilles, K. (2009). Receptor architecture of human cingulate cortex: Evaluation of the four-region neurobiological model. *Human brain mapping*, 30(8):2336–2355.

[114] Palomero-Gallagher, N. and Zilles, K. (2018). Cyto-and receptor architectonic mapping of the human brain. In *Handbook of clinical neurology*, volume 150, pages 355–387. Elsevier.

[115] Palomero-Gallagher, N. and Zilles, K. (2019). Cortical layers: Cyto-, myelo-, receptor-and synaptic architecture in human cortical areas. *Neuroimage*, 197:716–741.

[116] Paquola, C., De Wael, R. V., Wagstyl, K., Bethlehem, R. A., Hong, S.-J., Seidlitz, J., Bullmore, E. T., Evans, A. C., Misic, B., Margulies, D. S., et al. (2019). Microstructural and functional gradients are increasingly dissociated in transmodal cortices. *PLoS biology*, 17(5):e3000284.

[117] Pinheiro, E. S. D. S., Queirós, F. C. d., Montoya, P., Santos, C. L., Nascimento, M. A. d., Ito, C. H., Silva, M., Nunes Santos, D. B., Benevides, S., Miranda, J. G. V., et al. (2016). Electroencephalographic patterns in chronic pain: a systematic review of the literature. *PloS one*, 11(2):e0149085.

[118] Pittenger, C., Adams Jr, T. G., Gallezot, J.-D., Crowley, M. J., Nabulsi, N., Ropchan, J., Gao, H., Kichuk, S. A., Simpson, R., Billingslea, E., et al. (2016). Ocd is associated with an altered association between sensorimotor gating and cortical and subcortical 5-ht1b receptor binding. *Journal of affective disorders*, 196:87–96.

[119] Ploner, M., Sorg, C., and Gross, J. (2017). Brain rhythms of pain. *Trends in cognitive sciences*, 21(2):100–110.

[120] Poldrack, R. A., Kittur, A., Kalar, D., Miller, E., Seppa, C., Gil, Y., Parker, D. S., Sabb, F. W., and Bilder, R. M. (2011). The cognitive atlas: toward a knowledge foundation for cognitive neuroscience. *Frontiers Neuroinform*, 5:17.

[121] Radhakrishnan, R., Matuskey, D., Nabulsi, N., Gaiser, E., Gallezot, J.-D., Henry, S., Planeta, B., Lin, S.-f., Ropchan, J., Huang, Y., et al. (2020). In vivo 5-ht6 and 5-ht2a receptor availability in antipsychotic treated schizophrenia patients vs. unmedicated healthy humans measured with [11c] gsk215083 pet. *Psychiatry Research: Neuroimaging*, 295:111007.

[122] Radhakrishnan, R., Nabulsi, N., Gaiser, E., Gallezot, J.-D., Henry, S., Planeta, B., Lin, S.-f., Ropchan, J., Williams, W., Morris, E., et al. (2018). Age-related change in 5-ht6 receptor availability in healthy male volunteers measured with 11c-gsk215083 pet. *Journal of Nuclear Medicine*, 59(9):1445–1450.

[123] Radhakrishnan, R., Skosnik, P. D., Ranganathan, M., Naganawa, M., Toyonaga, T., Finnema, S., Hillmer, A. T., Esterlis, I., Huang, Y., Nabulsi, N., et al. (2021). In vivo evidence of lower synaptic vesicle density in schizophrenia. *Molecular Psychiatry*, pages 1–9.

[124] Ranganathan, M., Cortes-Briones, J., Radhakrishnan, R., Thurnauer, H., Planeta, B., Skosnik, P., Gao, H., Labaree, D., Neumeister, A., Pittman, B., et al. (2016). Reduced brain cannabinoid receptor availability in schizophrenia. *Biological psychiatry*, 79(12):997–1005.

[125] Richiardi, J., Altmann, A., Milazzo, A.-C., Chang, C., Chakravarty, M. M., Banaschewski, T., Barker, G. J., Bokde, A. L., Bromberg, U., Büchel, C., et al. (2015). Correlated gene expression supports synchronous activity in brain networks. *Science*, 348(6240):1241–1244.

[126] Rinne, J., Anichtchik, O., Eriksson, K., Kaslin, J., Tuomisto, L., Kalimo, H., Röyttä, M., and Panula, P. (2002). Increased brain histamine levels in parkinson's disease but not in multiple system atrophy. *Journal of neurochemistry*, 81(5):954–960.

[127] Robbins, T. W. and Arnsten, A. (2009). The neuropsychopharmacology of fronto-executive function: monoaminergic modulation. *Annual review of neuroscience*, 32:267–287.

[128] Roberts, J. A., Perry, A., Lord, A. R., Roberts, G., Mitchell, P. B., Smith, R. E., Calamante, F., and Breakspear, M. (2016). The contribution of geometry to the human connectome. *Neuroimage*, 124:379–393.

[129] Ruhé, H. G., Mason, N. S., and Schene, A. H. (2007). Mood is indirectly related to serotonin, norepinephrine and dopamine levels in humans: a meta-analysis of monoamine depletion studies. *Molecular psychiatry*, 12(4):331–359.

[130] Sagvolden, T., Johansen, E. B., Wøien, G., Walaas, S. I., Storm-Mathisen, J., Bergersen, L. H., Hvalby, Ø., Jensen, V., Aase, H., Russell, V. A., et al. (2009). The spontaneously hypertensive rat model of adhd–the importance of selecting the appropriate reference strain. *Neuropharmacology*, 57(7-8):619–626.

[131] Salimi-Khorshidi, G., Douaud, G., Beckmann, C. F., Glasser, M. F., Griffanti, L., and Smith, S. M. (2014). Automatic denoising of functional mri data: combining independent component analysis and hierarchical fusion of classifiers. *Neuroimage*, 90:449–468.

[132] Salvador, R., Suckling, J., Coleman, M. R., Pickard, J. D., Menon, D., and Bullmore, E. (2005). Neurophysiological architecture of functional magnetic resonance images of human brain. *Cerebral cortex*, 15(9):1332–1342.

[133] Sanchez-Rangel, E., Gallezot, J.-D., Yeckel, C. W., Lam, W., Belfort-DeAguiar, R., Chen, M.-K., Carson, R. E., Sherwin, R., and Hwang, J. J. (2020). Norepinephrine transporter availability in brown fat is reduced in obesity: a human pet study with [11 c] mrb. *International Journal of Obesity*, 44(4):964–967.

[134] Sandiego, C. M., Gallezot, J.-D., Lim, K., Ropchan, J., Lin, S.-f., Gao, H., Morris, E. D., and Cosgrove, K. P. (2015). Reference region modeling approaches for amphetamine challenge studies with [11c] flb 457 and pet. *Journal of Cerebral Blood Flow & Metabolism*, 35(4):623–629.

[135] Sandiego, C. M., Matuskey, D., Lavery, M., McGovern, E., Huang, Y., Nabulsi, N., Ropchan, J., Picciotto, M. R., Morris, E. D., McKee, S. A., et al. (2018). The effect of treatment with guanfacine, an alpha2 adrenergic agonist, on dopaminergic tone in tobacco smokers: An [11 c] flb457 pet study. *Neuropsychopharmacology*, 43(5):1052–1058.

[136] Saricicek, A., Chen, J., Planeta, B., Ruf, B., Subramanyam, K., Maloney, K., Matuskey, D., Labaree, D., Deserno, L., Neumeister, A., et al. (2015). Test–retest reliability of the novel 5-ht 1b receptor pet radioligand [11 c] p943. *European journal of nuclear medicine and molecular imaging*, 42(3):468–477.

[137] Sasaki, T., Ito, H., Kimura, Y., Arakawa, R., Takano, H., Seki, C., Kodaka, F., Fujie, S., Takahata, K., Nogami, T., et al. (2012). Quantification of dopamine transporter in human brain using pet with 18f-fe-pe2i. *Journal of Nuclear Medicine*, 53(7):1065–1073.

[138] Savli, M., Bauer, A., Mitterhauser, M., Ding, Y.-S., Hahn, A., Kroll, T., Neumeister, A., Haeusler, D., Ungersboeck, J., Henry, S., et al. (2012). Normative database of the serotonergic system in healthy subjects using multi-tracer pet. *Neuroimage*, 63(1):447–459.

[139] Schaefer, A., Kong, R., Gordon, E. M., Laumann, T. O., Zuo, X.-N., Holmes, A. J., Eickhoff, S. B., and Yeo, B. T. (2018). Local-global parcellation of the human cerebral cortex from intrinsic functional connectivity mri. *Cerebral cortex*, 28(9):3095–3114.

[140] Schmaal, L., Hibar, D., Sämann, P. G., Hall, G., Baune, B., Jahanshad, N., Cheung, J., Van Erp, T., Bos, D.,

Ikram, M. A., et al. (2017). Cortical abnormalities in adults and adolescents with major depression based on brain scans from 20 cohorts worldwide in the enigma major depressive disorder working group. *Molecular psychiatry*, 22(6):900–909.

[141] Schoenberger, M., Schroeder, F. A., Placzek, M. S., Carter, R. L., Rosen, B. R., Hooker, J. M., and Sander, C. Y. (2018). In vivo [18f] ge-179 brain signal does not show nmda-specific modulation with drug challenges in rodents and nonhuman primates. *ACS chemical neuroscience*, 9(2):298–305.

[142] Schwartz, J.-C. (2011). The histamine h3 receptor: from discovery to clinical trials with pitolisant. *British journal of pharmacology*, 163(4):713–721.

[143] Seaman, K. L., Smith, C. T., Juarez, E. J., Dang, L. C., Castrellon, J. J., Burgess, L. L., San Juan, M. D., Kundzicz, P. M., Cowan, R. L., Zald, D. H., et al. (2019). Differential regional decline in dopamine receptor availability across adulthood: Linear and nonlinear effects of age. *Human brain mapping*, 40(10):3125–3138.

[144] Seguin, C., Sporns, O., Zalesky, A., Calamante, F., et al. (2022). Network communication models narrow the gap between the modular organization of structural and functional brain networks. *bioRxiv*.

[145] Seidlitz, J., Nadig, A., Liu, S., Bethlehem, R. A., Vértes, P. E., Morgan, S. E., Váša, F., Romero-Garcia, R., Lalonde, F. M., Clasen, L. S., et al. (2020). Transcriptomic and cellular decoding of regional brain vulnerability to neurodevelopmental disorders. *Nature Communications*, .(.):.

[146] Seidlitz, J., Váša, F., Shinn, M., Romero-Garcia, R., Whitaker, K. J., Vértes, P. E., Wagstyl, K., Reardon, P. K., Clasen, L., Liu, S., et al. (2018). Morphometric similarity networks detect microscale cortical organization and predict inter-individual cognitive variation. *Neuron*, 97(1):231–247.

[147] Shafiei, G., Baillet, S., and Misic, B. (2021). Mapping electromagnetic networks to haemodynamic networks in the human brain. *bioRxiv*.

[148] Shafiei, G., Markello, R. D., De Wael, R. V., Bernhardt, B. C., Fulcher, B. D., and Misic, B. (2020). Topographic gradients of intrinsic dynamics across neocortex. *Elife*, 9:e62116.

[149] Shine, J. M. (2019). Neuromodulatory influences on integration and segregation in the brain. *Trends in cognitive sciences*, 23(7):572–583.

[150] Shine, J. M., Aburn, M. J., Breakspear, M., and Poldrack, R. A. (2018). The modulation of neural gain facilitates a transition between functional segregation and integration in the brain. *Elife*, 7:e31130.

[151] Shine, J. M., Breakspear, M., Bell, P. T., Martens, K. A. E., Shine, R., Koyejo, O., Sporns, O., and Poldrack, R. A. (2019). Human cognition involves the dynamic integration of neural activity and neuromodulatory systems. *Nat Neurosci*, 22(2):289–296.

[152] Shine, J. M., Müller, E. J., Munn, B., Cabral, J., Moran, R. J., and Breakspear, M. (2021). Computational models link cellular mechanisms of neuromodulation to large-scale neural dynamics. *Nature neuroscience*, 24(6):765–776.

[153] Shinn, M., Hu, A., Turner, L., Noble, S., Achard, S., Anticevic, A., Scheinost, D., Constable, R. T., Lee, D., Bullmore, E. T., et al. (2021). Spatial and temporal autocorrelation weave human brain networks. *bioRxiv*.

[154] Slifstein, M., Van De Giessen, E., Van Snellenberg, J., Thompson, J. L., Narendran, R., Gil, R., Hackett, E., Girgis, R., Ojeil, N., Moore, H., et al. (2015). Deficits in prefrontal cortical and extrastriatal dopamine release in schizophrenia: a positron emission tomographic functional magnetic resonance imaging study. *JAMA psychiatry*, 72(4):316–324.

[155] Smart, K., Cox, S. M., Scala, S. G., Tippler, M., Jaworska, N., Boivin, M., Séguin, J. R., Benkelfat, C., and Leyton, M. (2019). Sex differences in [11 c] abp688 binding: a positron emission tomography study of mglu5 receptors. *European journal of nuclear medicine and molecular imaging*, 46(5):1179–1183.

[156] Smart, K., Liu, H., Matuskey, D., Chen, M.-K., Torres, K., Nabulsi, N., Labaree, D., Ropchan, J., Hillmer, A. T., Huang, Y., et al. (2021). Binding of the synaptic vesicle radiotracer [11c] ucb-j is unchanged during functional brain activation using a visual stimulation task. *Journal of Cerebral Blood Flow & Metabolism*, 41(5):1067–1079.

[157] Smith, C. T., Crawford, J. L., Dang, L. C., Seaman, K. L., San Juan, M. D., Vijay, A., Katz, D. T., Matuskey, D., Cowan, R. L., Morris, E. D., et al. (2019). Partial-volume correction increases estimated dopamine d2-like receptor binding potential and reduces adult age differences. *Journal of Cerebral Blood Flow & Metabolism*, 39(5):822–833.

[158] Smith, R. E., Tournier, J.-D., Calamante, F., and Connelly, A. (2015). Sift2: Enabling dense quantitative assessment of brain white matter connectivity using streamlines tractography. *Neuroimage*, 119:338–351.

[159] Sporns, O. (2013). Network attributes for segregation and integration in the human brain. *Current opinion in neurobiology*, 23(2):162–171.

[160] Sporns, O. and Betzel, R. F. (2016). Modular brain networks. *Annual review of psychology*, 67:613–640.

[161] Starr, M. S. (1996). The role of dopamine in epilepsy. *Synapse*, 22(2):159–194.

[162] Stępnicki, P., Kondej, M., and Kaczor, A. A. (2018). Current concepts and treatments of schizophrenia. *Molecules*, 23(8):2087.

[163] Suárez, L. E., Markello, R. D., Betzel, R. F., and Misic, B. (2020). Linking structure and function in macroscale brain networks. *Trends Cogn Sci*.

[164] Sultzer, D. L., Lim, A. C., Gordon, H. L., Yarns, B. C., and Melrose, R. J. (2022). Cholinergic receptor binding in unimpaired older adults, mild cognitive impairment, and alzheimer's disease dementia. *Alzheimer's research & therapy*, 14(1):1–15.

[165] Sun, D., Ching, C. R., Lin, A., Forsyth, J. K., Kushan, L., Vajdi, A., Jalbrzikowski, M., Hansen, L., Villalon-Reina, J. E., Qu, X., et al. (2020). Large-scale mapping of cortical alterations in 22q11. 2 deletion syndrome: convergence with idiopathic psychosis and effects of deletion size. *Molecular psychiatry*, 25(8):1822–1834.

[166] Tadel, F., Baillet, S., Mosher, J. C., Pantazis, D., and Leahy, R. M. (2011). Brainstorm: a user-friendly application for meg/eeg analysis. *Computational intelligence and neuroscience*, 2011.

[167] Talbot, P. S., Slifstein, M., Hwang, D.-R., Huang, Y., Scher, E., Abi-Dargham, A., and Laruelle, M. (2012). Extended characterisation of the serotonin 2a (5-ht2a) receptor-selective pet radiotracer 11c-mdl100907 in humans: quantitative analysis, test–retest reproducibility, and vulnerability to endogenous 5-ht tone. *Neuroimage*,

59(1):271–285.

[168] Theodoni, P., Majka, P., Reser, D. H., Wójcik, D. K., Rosa, M. G., and Wang, X.-J. (2022). Structural attributes and principles of the neocortical connectome in the marmoset monkey. *Cerebral Cortex*, 32(1):15–28.

[169] Thompson, P. M., Jahanshad, N., Ching, C. R., Salminen, L. E., Thomopoulos, S. I., Bright, J., Baune, B. T., Bertolín, S., Bralten, J., Bruin, W. B., et al. (2020). Enigma and global neuroscience: A decade of large-scale studies of the brain in health and disease across more than 40 countries. *Translational psychiatry*, 10(1):1–28.

[170] Tournier, J. D., Calamante, F., Connelly, A., et al. (2010). Improved probabilistic streamlines tractography by 2nd order integration over fibre orientation distributions. In *Proceedings of the international society for magnetic resonance in medicine*, volume 1670. John Wiley & Sons, Inc. New Jersey, USA.

[171] Tournier, J.-D., Smith, R., Raffelt, D., Tabbara, R., Dhollander, T., Pietsch, M., Christiaens, D., Jeurissen, B., Yeh, C.-H., and Connelly, A. (2019). Mrtrix3: A fast, flexible and open software framework for medical image processing and visualisation. *Neuroimage*, 202:116137.

[172] Turtonen, O., Saarinen, A., Nummenmaa, L., Tuominen, L., Tikka, M., Armio, R.-L., Hautamäki, A., Laurikainen, H., Raitakari, O., Keltikangas-Järvinen, L., et al. (2021). Adult attachment system links with brain mu opioid receptor availability in vivo. *Biological Psychiatry: Cognitive Neuroscience and Neuroimaging*, 6(3):360–369.

[173] Vadodaria, K. C., Stern, S., Marchetto, M. C., and Gage, F. H. (2018). Serotonin in psychiatry: in vitro disease modeling using patient-derived neurons. *Cell and tissue research*, 371(1):161–170.

[174] van den Brink, R. L., Pfeffer, T., and Donner, T. H. (2019). Brainstem modulation of large-scale intrinsic cortical activity correlations. *Frontiers in human neuroscience*, 13:340.

[175] Van den Heuvel, M. P., Bullmore, E. T., and Sporns, O. (2016). Comparative connectomics. *Trends in cognitive sciences*, 20(5):345–361.

[176] Van Erp, T. G., Walton, E., Hibar, D. P., Schmaal, L., Jiang, W., Glahn, D. C., Pearlson, G. D., Yao, N., Fukunaga, M., Hashimoto, R., et al. (2018). Cortical brain abnormalities in 4474 individuals with schizophrenia and 5098 control subjects via the enhancing neuro imaging genetics through meta analysis (enigma) consortium. *Biological psychiatry*, 84(9):644–654.

[177] Van Essen, D. C., Smith, S. M., Barch, D. M., Behrens, T. E., Yacoub, E., Ugurbil, K., Consortium, W.-M. H., et al. (2013). The wu-minn human connectome project: an overview. *Neuroimage*, 80:62–79.

[178] van Galen, K. A., Ter Horst, K. W., and Serlie, M. J. (2021). Serotonin, food intake, and obesity. *Obesity Reviews*, page e13210.

[179] Van Rooij, D., Anagnostou, E., Arango, C., Auzias, G., Behrmann, M., Busatto, G. F., Calderoni, S., Daly, E., Deruelle, C., Di Martino, A., et al. (2018). Cortical and subcortical brain morphometry differences between patients with autism spectrum disorder and healthy individuals across the lifespan: results from the enigma asd working group. *American Journal of Psychiatry*, 175(4):359–369.

[180] Vasa, F. and Misic, B. (2022). Null models in network neuroscience. *Nat Rev Neurosci*.

[181] Vázquez-Rodríguez, B., Suárez, L. E., Markello, R. D., Shafiei, G., Paquola, C., Hagmann, P., Van Den Heuvel, M. P., Bernhardt, B. C., Spreng, R. N., and Misic, B. (2019). Gradients of structure–function tethering across neocortex. *Proceedings of the National Academy of Sciences*, 116(42):21219–21227.

[182] Veronese, M., Rizzo, G., Belzunce, M., Schubert, J., Searle, G., Whittington, A., Mansur, A., Dunn, J., Reader, A., Gunn, R. N., et al. (2021). Reproducibility of findings in modern pet neuroimaging: insight from the nrm2018 grand challenge. *Journal of Cerebral Blood Flow & Metabolism*, page 0271678X211015101.

[183] Vézquez-Rodríguez, B., Liu, Z.-Q., Hagmann, P., and Misic, B. (2020). Signal propagation via cortical hierarchies. *Network Neuroscience*, 4(4):1072–1090.

[184] Vijay, A., Wang, S., Worhunsky, P., Zheng, M.-Q., Nabulsi, N., Ropchan, J., Krishnan-Sarin, S., Huang, Y., and Morris, E. D. (2016). Pet imaging reveals sex differences in kappa opioid receptor availability in humans, in vivo. *American journal of nuclear medicine and molecular imaging*, 6(4):205.

[185] Wagstyl, K., Larocque, S., Cucurull, G., Lepage, C., Cohen, J. P., Bludau, S., Palomero-Gallagher, N., Lewis, L. B., Funck, T., Spitzer, H., et al. (2020). Bigbrain 3d atlas of cortical layers: Cortical and laminar thickness gradients diverge in sensory and motor cortices. *PLoS biology*, 18(4):e3000678.

[186] Wang, D., Tawfik, V. L., Corder, G., Low, S. A., François, A., Basbaum, A. I., and Scherrer, G. (2018). Functional divergence of delta and mu opioid receptor organization in cns pain circuits. *Neuron*, 98(1):90–108.

[187] Weiss, J. J., Calvi, R., Naganawa, M., Toyonaga, T., Farhadian, S. F., Chintanaphol, M., Chiarelle, J., Zheng, M.-Q., Ropchan, J., Huang, Y., Pietrzak, R. H., Carson, R. E., and Spudich, S. (2021). Preliminary in vivo evidence of reduced synaptic density in human immunodeficiency virus (hiv) despite antiretroviral therapy. *Clinical Infectious Diseases*, 73(8):1404–1411.

[188] Whelan, C. D., Altmann, A., Botía, J. A., Jahanshad, N., Hibar, D. P., Absil, J., Alhusaini, S., Alvim, M. K., Auvinen, P., Bartolini, E., et al. (2018). Structural brain abnormalities in the common epilepsies assessed in a worldwide enigma study. *Brain*, 141(2):391–408.

[189] Witjes, B., Baillet, S., Roy, M., Oostenveld, R., Huygen, F. J., and de Vos, C. C. (2021). Magnetoencephalography reveals increased slow-to-fast alpha power ratios in patients with chronic pain. *Pain reports*, 6(2).

[190] Yarkoni, T., Poldrack, R. A., Nichols, T. E., Van Essen, D. C., and Wager, T. D. (2011). Large-scale automated synthesis of human functional neuroimaging data. *Nat Meth*, 8(8):665.

[191] Yeo, B., Krienen, F. M., Sepulcre, J., Sabuncu, M. R., Lashkari, D., Hollinshead, M., Roffman, J. L., Smoller, J. W., Zöllei, L., Polimeni, J. R., et al. (2011). The organization of the human cerebral cortex estimated by intrinsic functional connectivity. *J Neurophysiol*, 106(3):1125–1165.

[192] Zakiniaeiz, Y., Hillmer, A. T., Matuskey, D., Nabulsi, N., Ropchan, J., Mazure, C. M., Picciotto, M. R., Huang, Y., McKee, S. A., Morris, E. D., et al. (2019). Sex differences in amphetamine-induced dopamine release in the dorsolateral prefrontal cortex of tobacco smokers. *Neuropsychopharmacology*, 44(13):2205–2211.

[193] Zilles, K., Bacha-Trams, M., Palomero-Gallagher, N., Amunts, K., and Friederici, A. D. (2015). Common molecular basis of the sentence comprehension network revealed by neurotransmitter receptor fingerprints. *Cortex*, 63:79–89.

[194] Zilles, K. and Palomero-Gallagher, N. (2017). Multiple transmitter receptors in regions and layers of the human cerebral cortex. *Frontiers in neuroanatomy*, 11:78.

[195] Zilles, K., Palomero-Gallagher, N., Grefkes, C., Scheperjans, F., Boy, C., Amunts, K., and Schleicher, A. (2002). Architectonics of the human cerebral cortex and transmitter receptor fingerprints: reconciling functional neuroanatomy and neurochemistry. *European neuropsychopharmacology*, 12(6):587–599.

[196] Zilles, K., Schleicher, A., Rath, M., and Bauer, A. (1988). Quantitative receptor autoradiography in the human brain. *Histochemistry*, 90(2):129–137.

[197] Zubieta, J.-K., Dannals, R. F., and Frost, J. J. (1999). Gender and age influences on human brain mu-opioid receptor binding measured by pet. *American Journal of Psychiatry*, 156(6):842–848.

[198] Zubieta, J.-K., Smith, Y. R., Bueller, J. A., Xu, Y., Kilbourn, M. R., Jewett, D. M., Meyer, C. R., Koeppe, R. A., and Stohler, C. S. (2001). Regional mu opioid receptor regulation of sensory and affective dimensions of pain. *Science*, 293(5528):311–315.

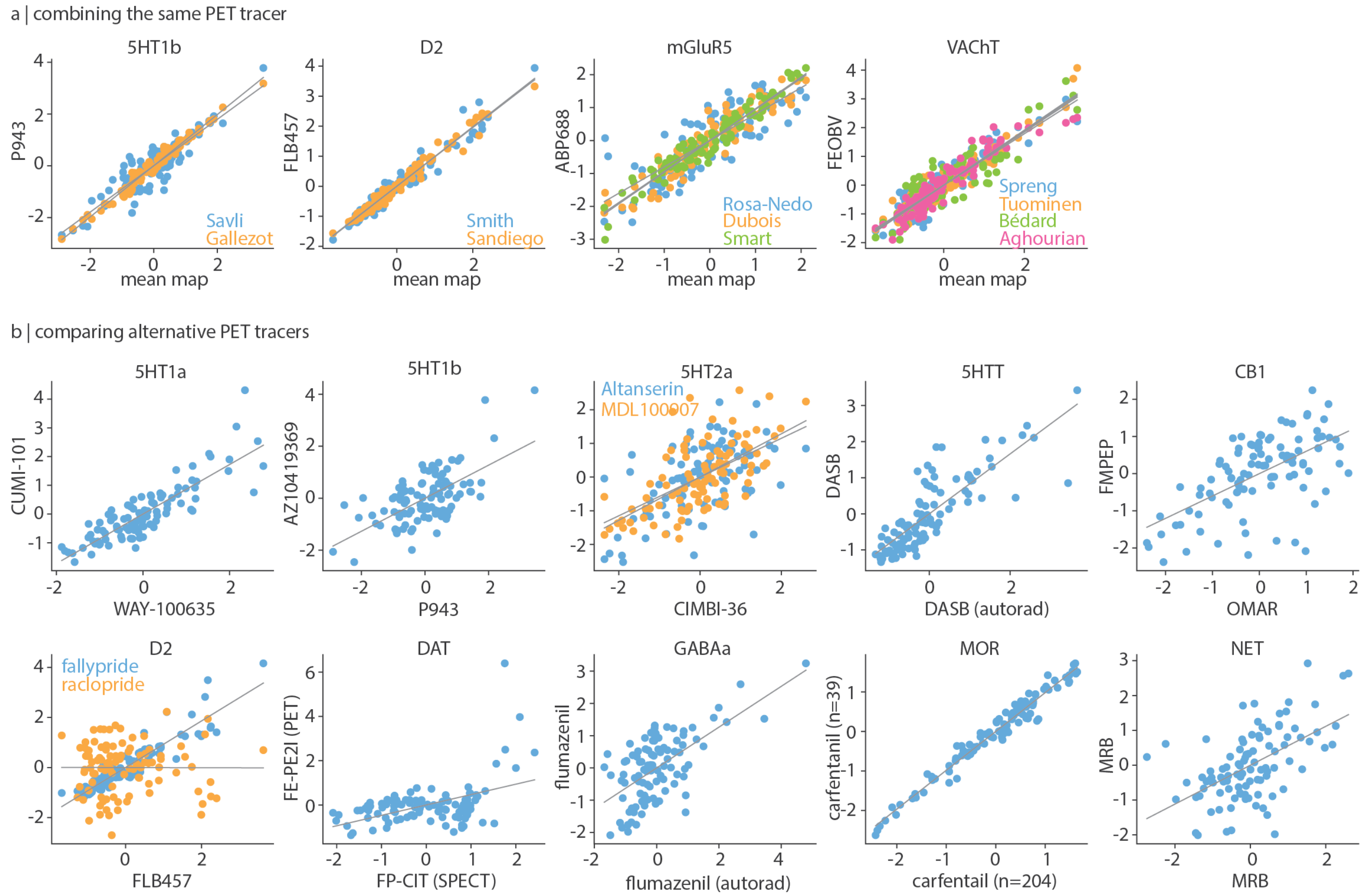

Figure S1. **Comparing different PET tracer images |** (a) PET maps of the same tracer were combined into a single average receptor/transporter map. Each individual PET tracer map (y-axis) is highly correlated to the mean map (x-axis). Names indicate the source of each PET map; see Table 1. (b) Multiple PET tracers were available for certain receptors/transporters. Scatter plots show the correlation between the selected tracer map (x-axis) and alternative maps (y-axis).

Receptor	Neurotransmitter	Excitatory/Inhibitory	Ionotropic/Metabotropic
AMPA	glutamate	excitatory	ionotropic
NMDA	glutamate	excitatory	ionotropic
Kainate	glutamate	excitatory	ionotropic
GABA$_A$	GABA	inhibitory	ionotropic
GABA$_{A/BZ}$	GABA	inhibitory	ionotropic
GABA$_B$	GABA	inhibitory	metabotropic
M$_1$	acetylcholine	excitatory	metabotropic
M$_2$	acetylcholine	inhibitory	metabotropic
M$_3$	acetylcholine	excitatory	metabotropic
$\alpha_4\beta_2$	acetylcholine	excitatory	ionotropic
α_1	norepinephrine	excitatory	metabotropic
α_2	norepinephrine	inhibitory	metabotropic
5-HT$_{1A}$	serotonin	inhibitory	metabotropic
5-HT$_2$	serotonin	excitatory	metabotropic
D$_1$	dopamine	excitatory	metabotropic

TABLE S1. **Neurotransmitter receptors included in the autoradiography dataset**

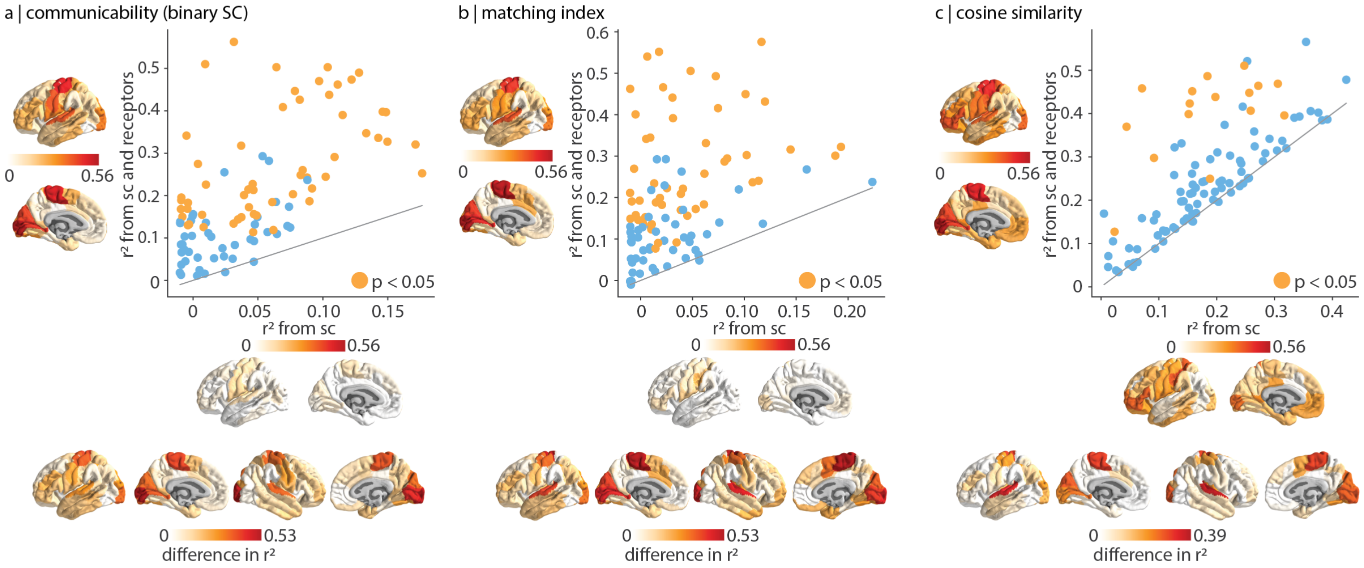

Figure S2. **Alternative representations of the structural connectome used in structure-function coupling |** Structure-function coupling was recomputed using (a) communicability calculated on the binary connectome, (b) matching index computed on the weighted connectome, and (c) cosine similarity of the weighted connectome.

action
adaptation
addiction
anticipation
anxiety
arousal
association
attention
autobiographical memory
balance
belief
categorization
cognitive control
communication
competition
concept
consciousness
consolidation
context
coordination
decision
decision making
detection
discrimination
distraction
eating
efficiency
effort
emotion
emotion regulation
empathy
encoding
episodic memory
expectancy
expertise
extinction
face recognition
facial expression
familiarity
fear
fixation
focus
gaze
goal
hyperactivity
imagery
impulsivity
induction
inference
inhibition
insight
integration
intelligence
intention
interference
judgment
knowledge
language
language comprehension
learning
listening
localization
loss
maintenance
manipulation
meaning
memory
memory retrieval
mental imagery
monitoring
mood
morphology
motor control
movement
multisensory
naming
navigation
object recognition
pain
perception
planning
priming
psychosis
reading
reasoning
recall
recognition
rehearsal
reinforcement learning
response inhibition
response selection
retention
retrieval
reward anticipation
rhythm
risk
rule
salience
search
selective attention
semantic memory
sentence comprehension
skill
sleep
social cognition
spatial attention
speech perception
speech production
strategy
strength
stress
sustained attention
task difficulty
thought
uncertainty
updating
utility
valence
verbal fluency
visual attention
visual perception
word recognition
working memory

TABLE S2. **Neurosynth terms |** Terms that overlapped between the Neurosynth database [190] and the Cognitive Atlas [120] were included in the PLS analysis.

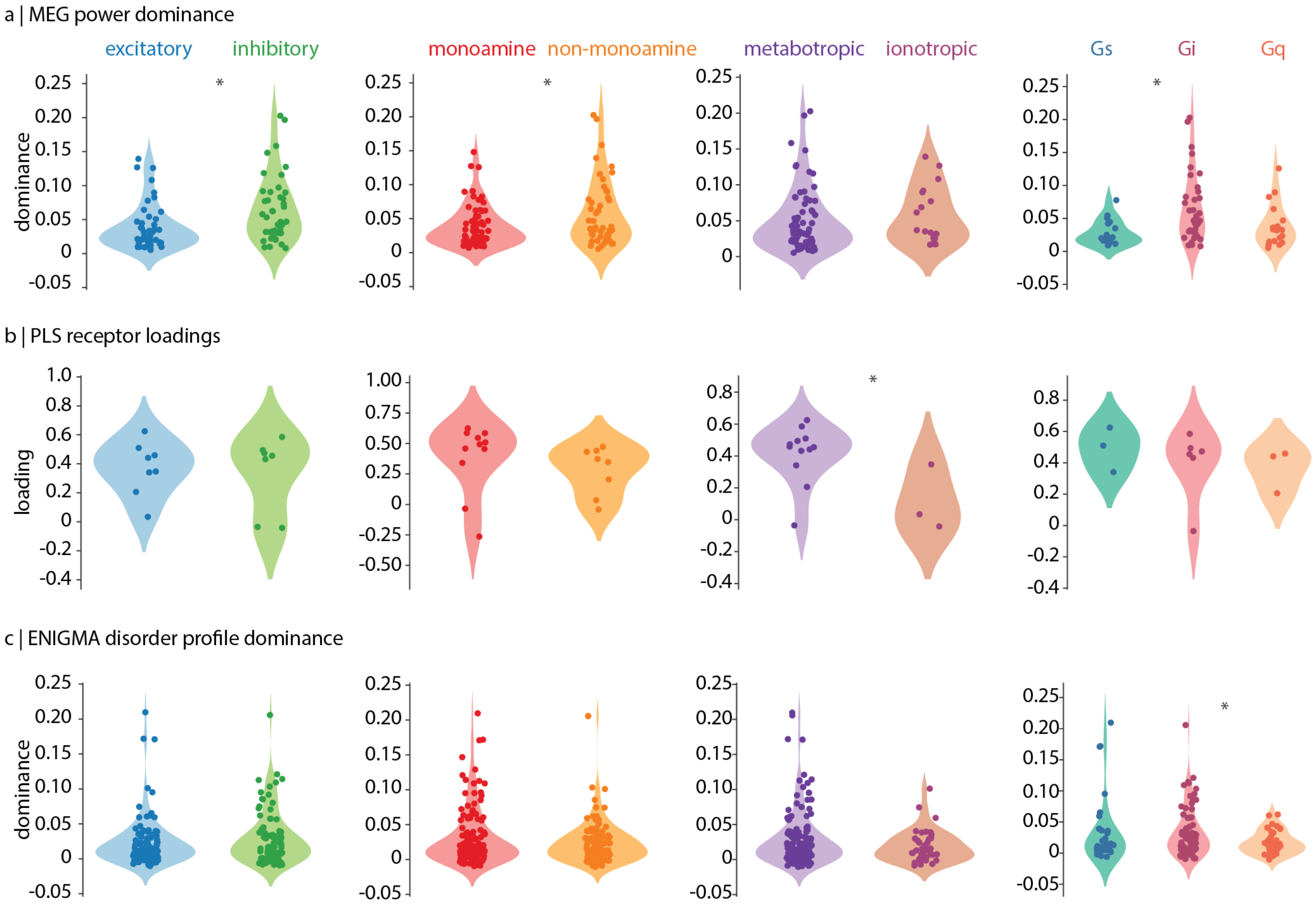

Figure S3. We compared the results from (a) the MEG power dominance analysis (Fig. 4 in the main text), (b) the PLS analysis with cognitive activations (Fig. 5 in the main text), and (c) the disease profile dominance analysis (Fig. 6 in the main text) across different classes of receptors (excitatory vs. inhibitory, monoamine vs. non-monoamine, metabotropic vs. ionotropic, Gs- vs. Gi- vs. Gq-coupled pathways). Asterisks indicate significance ($p < 0.05$, Welch's t-test)

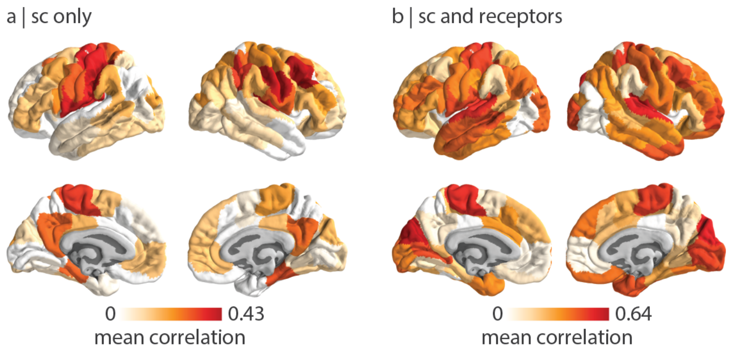

Figure S4. **Cross-validating structure-function coupling models |** At every brain region, distance-dependent cross-validation was applied to the (a) structure-function coupling model, and (b) the receptor-informed structure-function coupling model. The mean correlation between empirical and predicted values in the test set is shown on the brain surface.

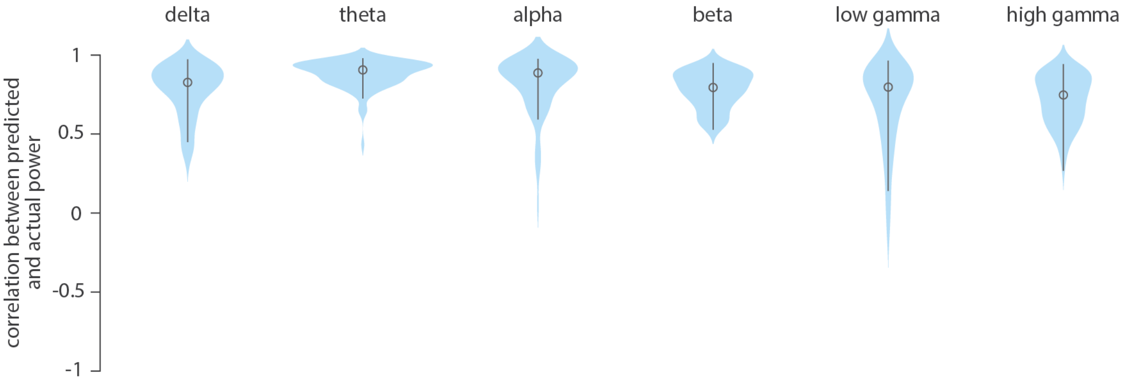

Figure S5. **Cross-validating models that predict MEG power distribution from receptor/transporter densities |** All six multilinear models between receptor/transporter densities and MEG power distributions were cross-validated using a distance-dependent method. This method selects the 25% of regions closest to a source-region as a training set and the remaining 75% of regions as the test set. The procedure is repeated for each brain region as the source region (68 iterations). We assessed the prediction by correlating predicted power to the empirical power in the test set.

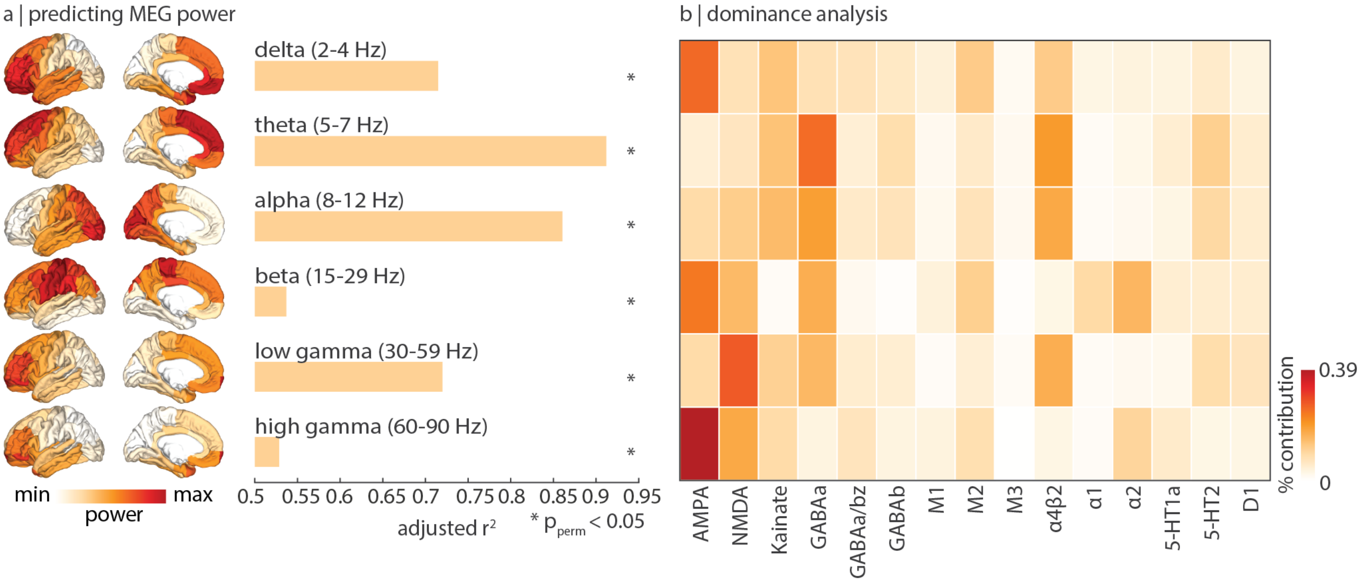

Figure S6. **Excitatory ionotropic receptor densities shape neural dynamics |** Multilinear regression models were fit between autoradiography-derived neurotransmitter receptor densities and MEG power, done analogously in Fig. 4. (a) Autoradiography-derived receptor densities map closely to neural dynamics. The significance of each model is assessed using a permutation test and is corrected for multiple comparisons (FDR). Asterisks denote significant models (FDR-corrected $p_{\text{perm}} < 0.05$ [15]). (b) Dominance analysis distributes the fit of the model across input variables such that the contribution of each variable can be assessed and compared to other input variables. The percent contribution of each input variable is defined as the variable's dominance normalized by the total fit (R^2_{adj}) of the model.

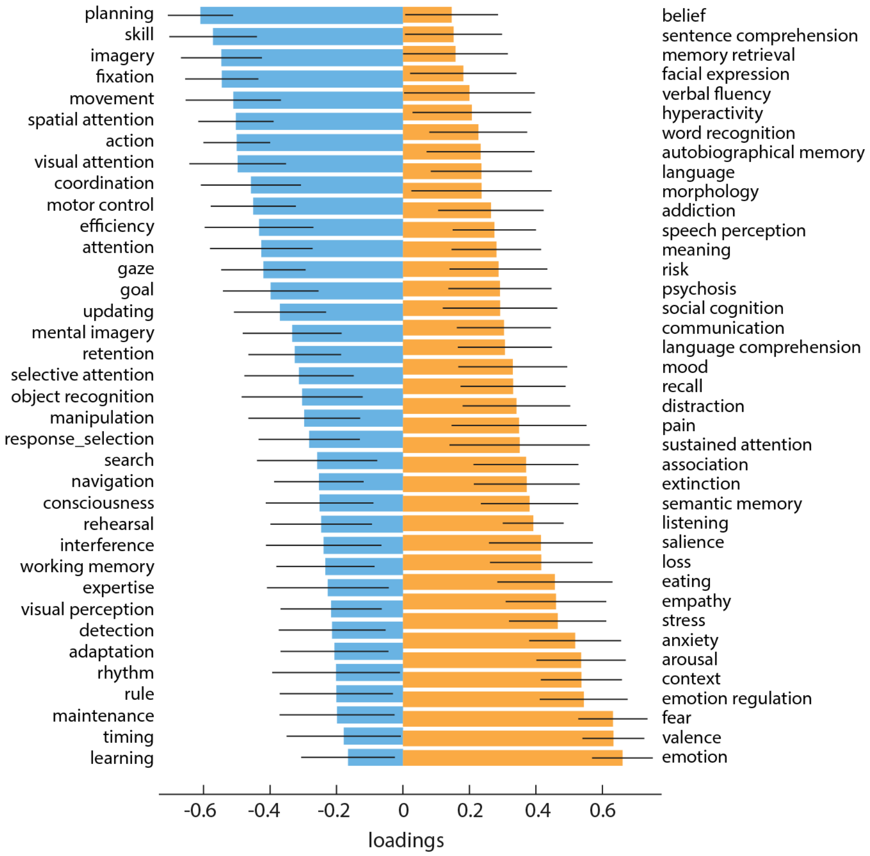

Figure S7. **Neurosynth cognitive loadings |** The loading for each cognitive process is calculated as the Pearson's correlation between functional activations across brain regions and PLS-derived receptor scores. Error bars indicate bootstrap-estimated 95% confidence intervals (10 000 bootstrap samples). All cognitive processes with a confidence interval that changes sign are excluded.

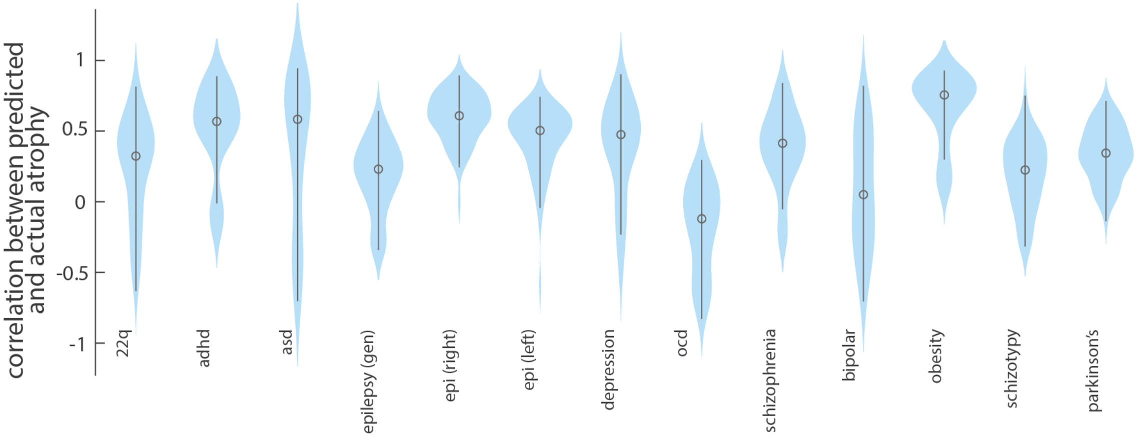

Figure S8. **Cross-validating models that predict disorder-specific cortical abnormality from receptor/transporter densities |** All thirteen multilinear models between receptor/transporter densities and disorder-specific cortical abnormality were cross-validated using a distance-dependent method. This method selects the 25% of regions closest to a source-region as a training set and the remaining 75% of regions as the test set. The procedure is repeated for each brain region as the source region (68 iterations). We assessed the prediction by correlating predicted atrophy to the empirical atrophy in the test set. Note that this analysis is conducted using the Desikan-Killiany atlas because this is the only representation of ENIGMA datasets [33].

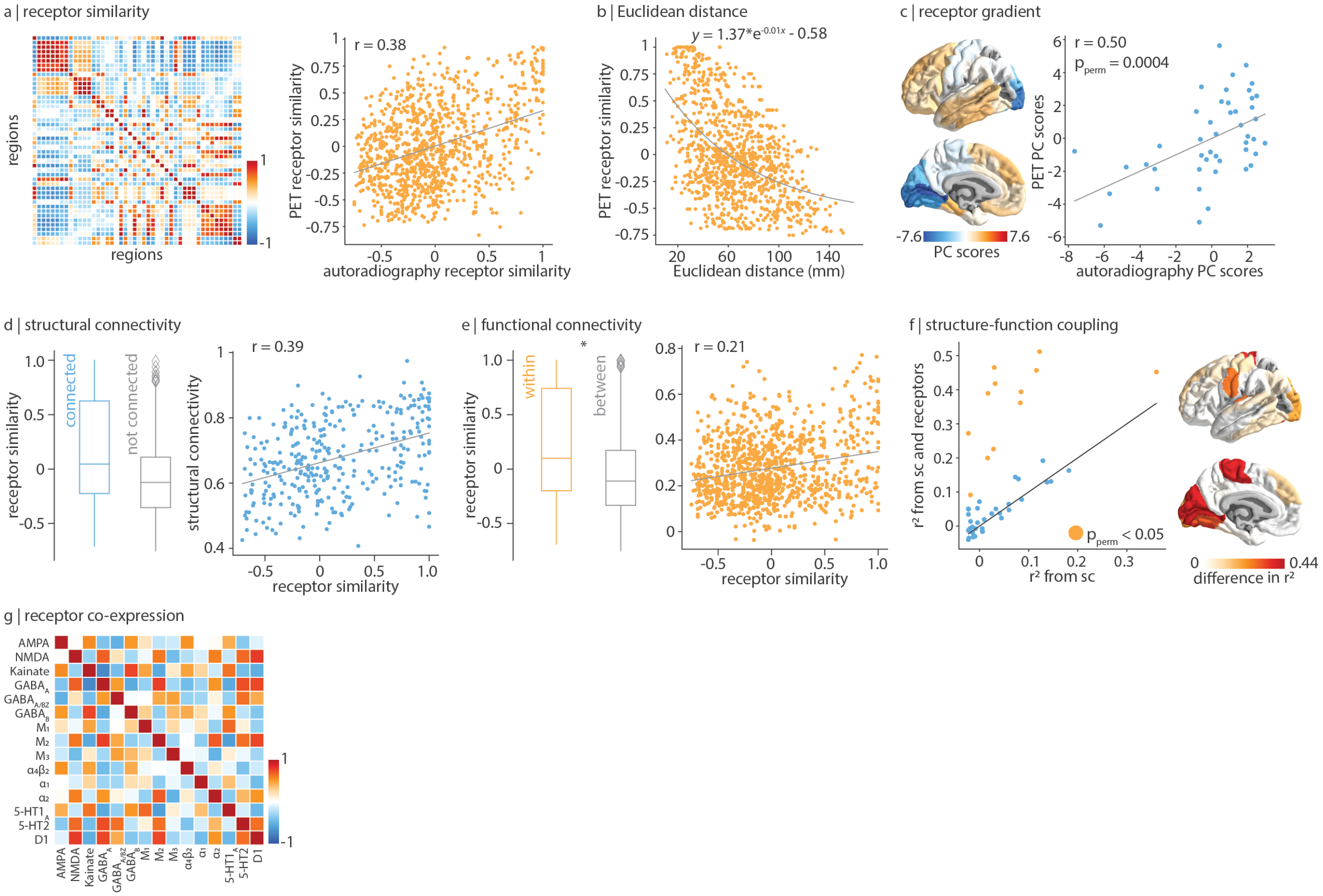

Figure S9. **Autoradiography-informed neurotransmitter receptor densities follow similar organizational principles as PET-informed neurotransmitter receptor densities |** Autoradiography images of fifteen neurotransmitter receptors across three post-mortem brains were acquired by Zilles and Palomero-Gallagher [194]. (a) The receptor similarity matrix is constructed by correlating receptor fingerprints at each pair of brain regions (left). PET-derived receptor similarity is correlated to autoradiography-derived receptor similarity (Pearson's $r(1033) = 0.38$, $p < 0.001$; right). (b) Receptor similarity decays exponentially with Euclidean distance. (c) The first principal component of autoradiography-derived receptor density (left brain plot) is non-significantly correlated with the first principal component of PET-derived receptor density ($r(44) = -0.50$, $p_{\text{spin}} = 0.06$, two-sided). (d) Receptor similarity is non-significantly greater between pairs of regions that are physically connected, against a degree- and edge-length-preserving null model (left; $p = 0.19$ [16]), and is significantly correlated with structural connectivity (Pearson's $r(329) = 0.39$, $p < 0.001$, right). (e) Receptor similarity is significantly greater in regions within the same functional network as opposed to between functional networks (left; $p_{\text{spin}} = 0.03$), and is correlated to functional connectivity (right; Pearson's $r(1033) = 0.21$, $p < 0.001$). (f) Consistent with PET-derived results, receptor similarity augments structure-function coupling in visual, paracentral, and somatomotor regions. (g) Receptor co-expression (Pearson's correlation) for every pair of receptors across 46 brain regions. Asterisks in panel (e) denote significance. Boxplots in (d) and (e) represent the 1st, 2nd (median) and 3rd quartiles, whiskers represent the non-outlier end-points of the distribution, and diamonds represent outliers.

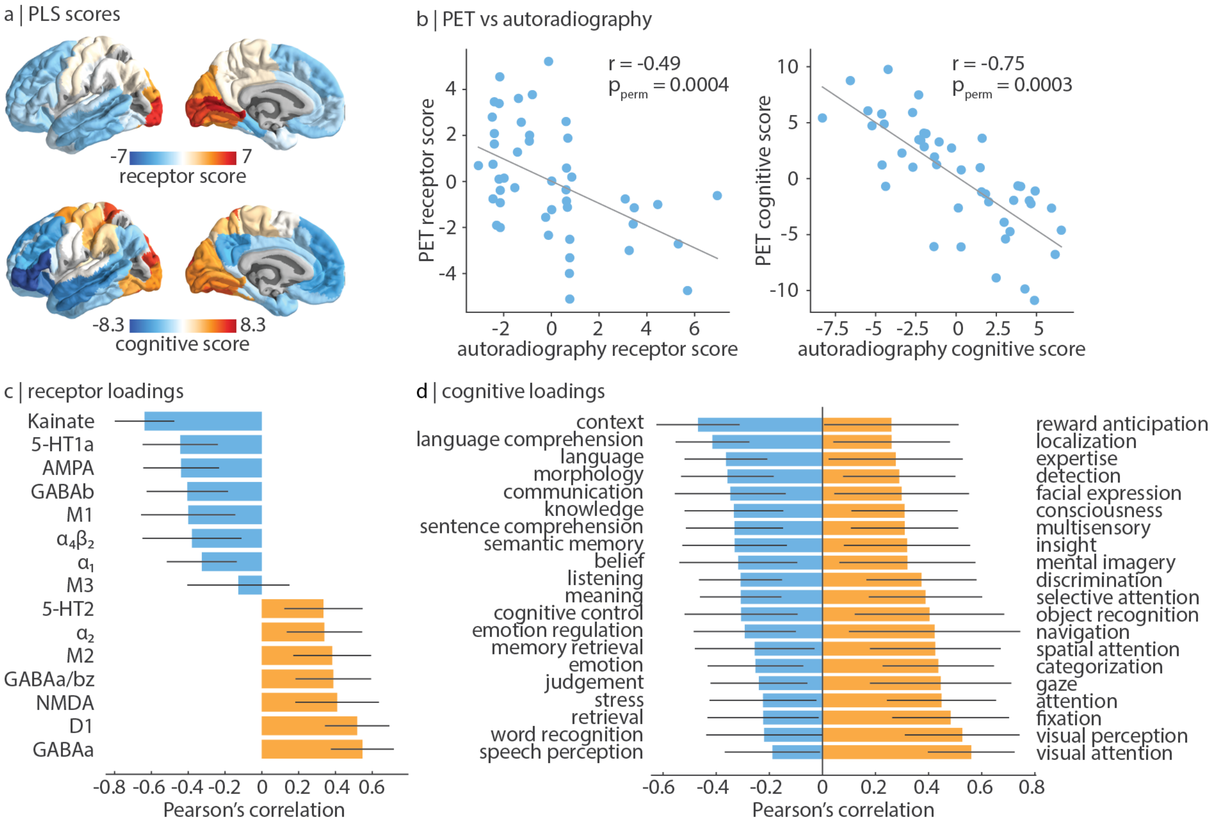

Figure S10. **Mapping autoradiography-derived receptors to cognition |** Partial least squares analysis was applied to autoradiography-derived receptor densities and Neurosynth-derived cognitive functional activations, done analogously in Fig. 5. (a) Receptor (top) and cognitive (bottom) score patterns follow a similar sensory-fugal gradient. (b) Autoradiography-derived PLS scores are correlated with PET-derived PLS scores. (c) Receptor loadings are defined as the Pearson's correlation between each receptor's distribution across the cortex and the PLS-derived receptor scores and can be interpreted as the contribution of each receptor to the latent variable. (c) Cognitive loadings are shown for all stable positively- and negatively-loaded cognitive processes. 95% confidence intervals are estimated for receptor and cognitive loadings using bootstrap resampling (10 000 repetitions).

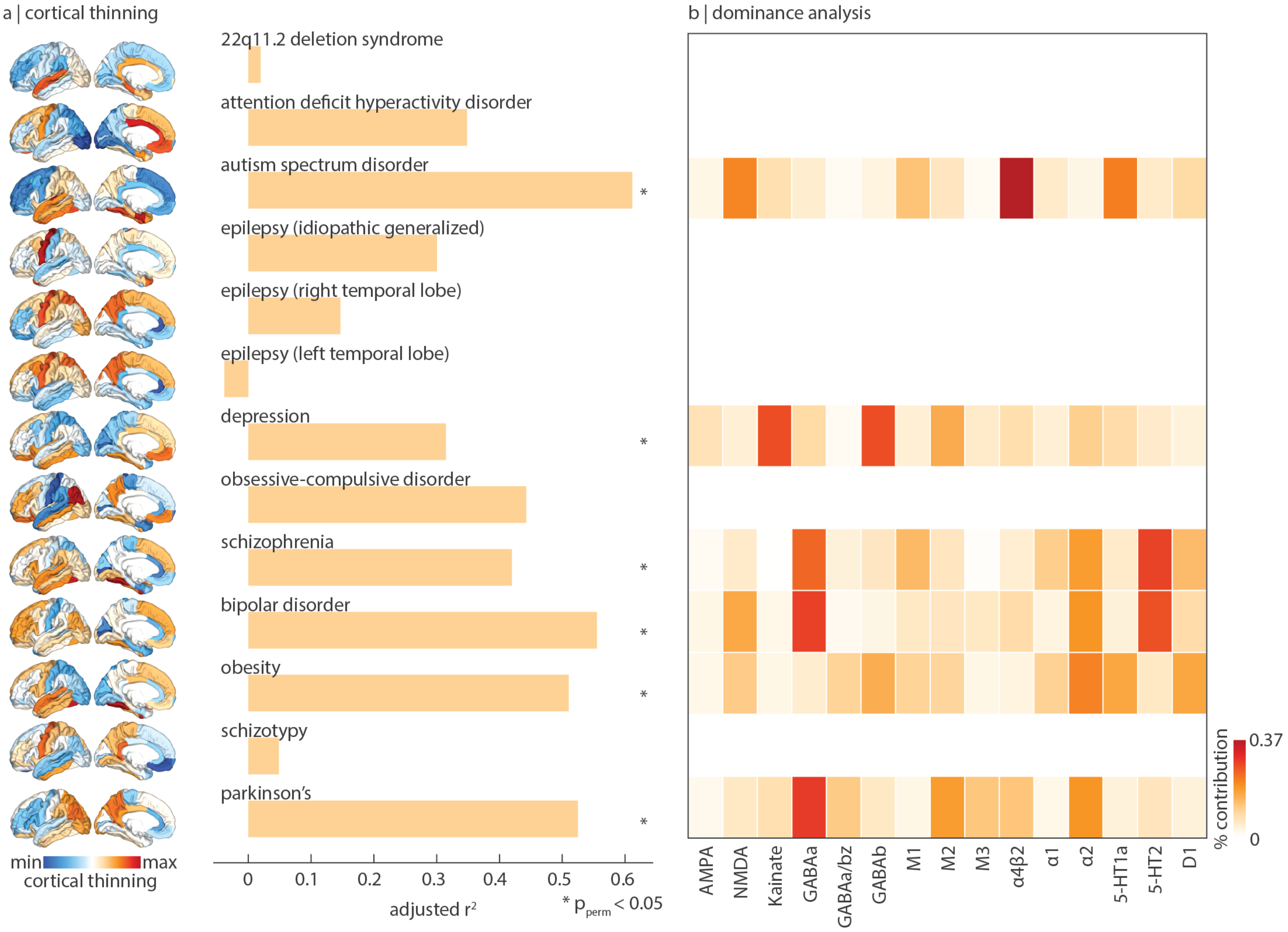

Figure S11. **Mapping autoradiography-derived receptors to disease vulnerability |** For each disorder, we fit a multilinear regression model between autoradiography-derived receptor densities and cortical abnormality, done analogously in Fig. 6. (a) Model fit (adjusted R^2) varies across disorders. The significance of each model is assessed using a permutation test and is corrected for multiple comparisons (FDR). Asterisks denote significant models (FDR-corrected $p_{\text{perm}} < 0.05$ [15]). (b) Dominance analysis distributes the fit of the model across input variables such that the contribution of each variable can be assessed and compared to other input variables. The percent contribution of each input variable is defined as the variable's dominance normalized by the total fit (R^2_{adj}) of the model. Note that this analysis is conducted using the Desikan-Killiany atlas because this is the only representation of ENIGMA datasets [33].

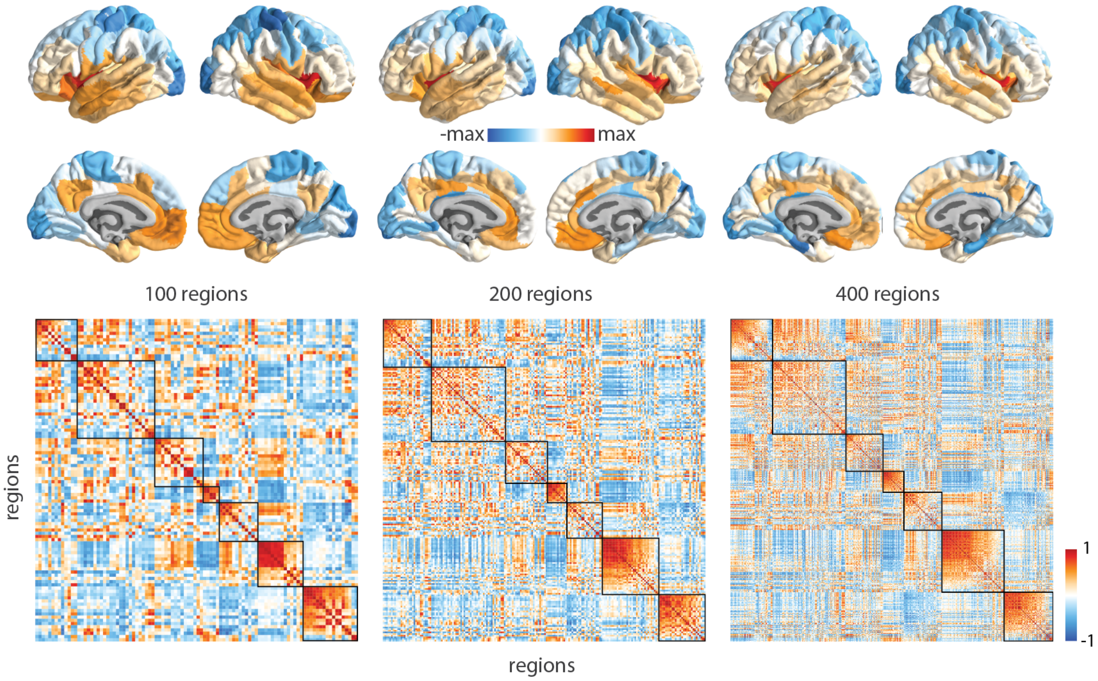

Figure S12. **Replicating results using different parcellation resolutions |** Top: first principal gradient of normalized neurotransmitter receptor/transporter density is consistent across three increasingly fine parcellation resolutions (100 regions (original), 200 regions, and 400 regions) [139]. Bottom: receptor similarity matrices also demonstrate high conformity across parcellation resolutions. Receptor similarity matrices are ordered by Yeo-Krienen intrinsic networks (order: frontoparietal, default mode, dorsal attention, limbic, ventral attention, somatomotor, visual) [191].

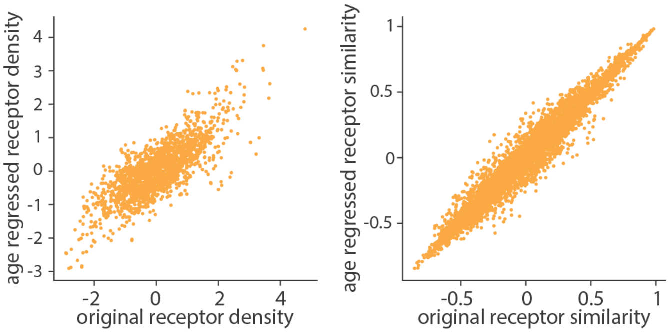

Figure S13. **Age has negligible effect on the reported findings |** To test age effects of the PET tracer images, we regressed out the relationship between mean age of each tracer map and z-scored receptor densities, at each brain region separately. Age has little impact on receptor density (left; Pearson's $r(4948) = 0.79$) and receptor similarity (right; Pearson's $r(4948) = 0.97$).